Article:
Evans, EL, Povstyan, OV, De Vecchis, D orcid.org/0000-0002-7732-5095 et al. (9 more authors) (2020) RBCs prevent rapid PIEZO1 inactivation and expose slow deactivation as a mechanism of DHS. Blood. ISSN 0006-4971

https://doi.org/10.1182/blood.2019004174

RBCs prevent rapid PIEZO1 inactivation and expose slow deactivation as a mechanism of DHS

Elizabeth L Evans[†1], Oleksandr V Povstyan[†1], Dario De Vecchis[1], Fraser Macrae[1], Laeticia Lichtenstein[1], T Simon Futers[1], Gregory Parsonage[1], Neil Humphreys[2], Antony Adamson[2], Antreas C Kalli*[1], Melanie J Ludlow*[1], David J Beech*[1]

[1]School of Medicine, University of Leeds, Leeds, England, UK. [2]Faculty of Biology, Medicine and Health, University of Manchester, AV Hill Building, Manchester M13 9PT, UK

[†]Equal contributors

*Authors for correspondence: Professor David Beech, Leeds Institute of Cardiovascular and Metabolic Medicine, School of Medicine, LIGHT Building, Clarendon Way, University of Leeds, Leeds LS2 9JT, UK. Email d.j.beech@leeds.ac.uk. Dr Melanie Ludlow, Leeds Institute of Cardiovascular and Metabolic Medicine, School of Medicine, LIGHT Building, Clarendon Way, University of Leeds, Leeds LS2 9JT, UK. Email m.j.ludlow@leeds.ac.uk. Dr Antreas Kalli, Leeds Institute of Cardiovascular and Metabolic Medicine, LIGHT Building, Clarendon Way, School of Medicine, University of Leeds, Leeds LS2 9JT, UK. E-mail a.kalli@leeds.ac.uk. Telephone +44 (0) 0113 343 7722.

The discovery of PIEZO proteins has enabled better understanding of how cells respond to mechanical force[1-3]. PIEZOs assemble to form ion channels that link force to cell behaviour via transmembrane cation flux[1,2,4]. Shortly after the initial PIEZO discoveries, associations of *PIEZO1* mutations with xerocytosis / dehydrated hereditary stomatocytosis (DHS)[4-15] and links to malarial resistance were suggested[16]. PIEZO1 channels are now an established feature of red blood cell (RBC) biology where they regulate intracellular Ca^{2+} and cell hydration in coordination with other mechanisms such as the Gardos channel[17-20]. However, studies of PIEZO1 reconstituted in cell lines have suggested that the channels activate within milliseconds and then inactivate (desensitize) completely within a few hundred milliseconds when rapidly stimulated by increases in membrane tension caused by pulling on the membrane or cell deformation via a probe[1,4,7,9,18]. DHS mutations have been found to slow the fast inactivation process, which represents gain-of-function[7-9,18]. It is, however, unclear how such rapid events are relevant to RBC physiology. Moreover, although the available data are limited because of the low prevalence of DHS, studies of RBCs from patients suggest sustained channel activity unlike that reported for PIEZO1 in cell lines[6,10,12,15]. Therefore we sought additional understanding through electrophysiological analysis of murine RBCs. To mechanically stimulate the channels we applied shear stress, a frictional force created physiologically by blood flow. To understand the impact of DHS mutation we generated the murine equivalent of one of the first-identified DHS mutations, M2225R[4,5,8,9].

In mouse PIEZO1, the equivalent of M2225R is M2241R. Molecular modelling and pharmacological analysis of overexpressed channels suggested suitability of mouse PIEZO1 as a model for human PIEZO1 (Supplemental Results and Figures S1-S2). Furthermore, 8 week-old mice homozygous for M2241R ($PIEZO1^{M\text{-}R/M\text{-}R}$) (Supplemental Results and Figures S3-S4) displayed features consistent with DHS that included stomatocytosis (Supplemental Figure S5), decreased osmotic fragility (Supplemental Figure S6), decreased haemoglobin, haematocrit and RBC count (Supplemental Table S1) and increased RBC and haemoglobin concentration distribution widths and percentage of reticulocytes (Supplemental Table S1). There were no significant changes in spleen weight (Supplemental Figure S7) or liver function tests (Supplemental Table S2). There were potential changes in plasma iron and total iron binding capacity that did not reach statistical significance but transferrin showed a small significant increase (Supplemental Table S2). $PIEZO1^{M\text{-}R/M\text{-}R}$ mice were born at slightly lower frequency than wildtype mice, suggesting a potential deleterious effect, but adult $PIEZO1^{M\text{-}R/M\text{-}R}$ mice appeared normal and body weight gain was not different from wildtype mice (Supplemental Figure S8). However, increased spleen weight in $PIEZO1^{M\text{-}R/M\text{-}R}$ mice at 22 weeks of age suggested the potential for age-related changes in phenotype (Supplemental Figure S7). All experiments henceforth focussed on mice at 8 weeks of age. Heterozygote mice ($PIEZO1^{WT/M\text{-}R}$) showed decrease in osmotic fragility but less than for $PIEZO1^{M\text{-}R/M\text{-}R}$ mice, which suggested intermediate phenotype (Supplemental Figure S6). $PIEZO1^{WT/M\text{-}R}$ mice were born at the expected Mendelian ratio (Supplemental Figure S8).

To understand the effect of M2241R on channel properties, patch-clamp electrophysiology was applied to RBCs freshly isolated from mice. For physiological relevance we first used the perforated-patch whole-cell configuration to achieve membrane potential measurements. Resting membrane potential data are provided in the Supplemental Information. For most experiments, constant current was injected to hyperpolarise RBCs to -80 mV and thereby maximise visibility of PIEZO1-related responses to fluid flow of 20 $\mu L.s^{-1}$, a rate that occurs in mice[21]. There was a small depolarisation to fluid flow in WT RBCs, consistent with the opening of PIEZO1 channels (Figure 1a) (mean data in Figure 1d). The depolarisation was sustained for at least 20 s. After flow ceased, membrane potential returned to its initial value (Figure 1a, d). Depolarisation tended to be larger in $PIEZO1^{WT/M\text{-}R}$ and was larger ($P < 0.05$) in $PIEZO1^{M\text{-}R/M\text{-}R}$ RBCs but the most striking difference was failure to recover after flow ceased (Figure 1b, c) (mean data in Figure 1d). To further investigate we switched to voltage-clamp mode. In WT RBCs, fluid flow caused inward current as expected, which then decayed slowly after about 10 s (Figure 1f) (mean data in Figure 1i). In $PIEZO1^{WT/M\text{-}R}$ and $PIEZO1^{M\text{-}R/M\text{-}R}$ RBCs, the initial response was similar to WT except the slow inactivation was mostly absent (Figure 1g, h). Most strikingly there was failure of current to recover after cessation of fluid flow (Figure 1g, h) (mean data in Figure 1i). GsMTx4, an inhibitor of PIEZO1 channel activity[22], abolished all depolarising and inward current activities (Figure 1e, j; Supplemental Figures S9 and S10). Intriguingly, wash-out of GsMTx4 from

mutant RBCs revealed recover to activity that was more like the activity of WT RBCs than mutant RBCs in the absence of toxin, suggesting potential to correct the mutant channel behaviour (Supplemental Figures S9 and S10).

To investigate more closely, single channel data were sought by recording from cell-attached membrane patches under voltage-clamp and applying short pressure pulses to the patch pipette to increase membrane tension. Occasionally there was only one unitary current level, suggesting only one channel in the patch (Figures 2a and 2e) but in most cases there were multiple channels (e.g., Figure 2c, g). PIEZO1 channels were identified by the signature unitary current amplitude[1] (Figure 2b, d, f and Supplemental Figure S11). In the WT exemplar shown, activity was evoked by the -80 and -90 mmHg pressure pulses but afterwards there were only infrequent openings, suggesting that this channel mostly deactivated (Figure 2a). The rarity of channel opening was seen particularly in the amplitude histogram, which indicated low frequency at -2.5 pA (channel open) relative to that at -0.5 pA (channel closed) (Figure 2b). In contrast, in PIEZO1$^{WT/M-R}$ and PIEZO1$^{M-R/M-R}$ RBCs there was identical unitary current amplitude but remarkably higher activity after termination of pressure pulses (Figure 2c-f). Histogram analysis highlighted the difference between WT and PIEZO1$^{WT/M-R}$ / PIEZO1$^{M-R/M-R}$ because the frequency of open-state activity (e.g., at -2.5, -2.7 and -2.4 pA) was high relative to the closed-state frequency (i.e., at -0.5, -0.7 and -0.4 pA) (Figure 2d, f *cf* Figure 2b). Patches containing multiple PIEZO1$^{M-R/M-R}$ channels in the same patch also showed the persistent high activity (Figure 2g). Summary analysis of multi-channel activity also supported the conclusion that persistent activity was greater in PIEZO1$^{WT/M-R}$ / PIEZO1$^{M-R/M-R}$ (Supplemental Figure S12). Unitary current events were abolished by GsMTx4 (Figure 2h).

The data suggest that RBCs provide a special environment for PIEZO1 that disables or greatly slows the rapid inactivation mechanism and confers importance of deactivation, which is a different mechanism from inactivation. In future studies it will be interesting to determine how the rapid inactivation gate is disabled or slowed in RBCs. Our work on endothelial PIEZO1 has suggested capability of sphingomyelinase to cause such effect[23]. Sphingomyelinase is known to regulate RBC membrane structure[24] and adhesion of eryptotic RBCs to endothelial cells[25]. It will also be interesting to determine the molecular mechanism of deactivation in PIEZO1, its sensitivity to other DHS mutations in the RBC context and the potential for correction by small-molecules. Such studies could have multiple benefits for better understanding RBC homeostasis and DHS and enable better appreciation of the mechanical biology of other blood-borne cells that normally live in an environment of dynamic shear stress.

ACKNOWLEDGEMENTS

Supported by Wellcome Trust Investigator and British Heart Foundation programme grants to D.J.B. and an Academy of Medical Sciences and Wellcome Trust Springboard Award to A.K.. E.L.E. was supported by a British Heart Foundation PhD Studentship. We thank the Blood Sciences Laboratory at Leeds General Infirmary for analysis of blood samples.

AUTHOR CONTRIBUTIONS

E.L.E., O.V.P., M.J.L, F.M. and L.L. performed experiments and data analysis. O.V.P. performed and analysed the patch-clamp recordings. D.DV. and A.K. generated the molecular models. M.J.L., N.H. and A.A. generated the PIEZO1$^{M-R/M-R}$ mouse. T.S.F. led the mouse breeding strategy. G.P. provided technical support. E.L.E., O.V.P., M.J.L. and D.J.B. designed the research. D.J.B. raised funds to support the work and wrote the paper with support from all authors.

DISCLOSURE OF CONFLICTS OF INTEREST

The authors declare no competing financial interests

DATA AVAILABILITY

Source Data are provided.

REFERENCES

1. Coste B, Mathur J, Schmidt M, et al. PIEZO1 and PIEZO2 are essential components of distinct mechanically-activated cation channels. *Science* 2010;330(6000):55-60.

2. Murthy SE, Dubin AE, Patapoutian A. PIEZOs thrive under pressure: mechanically activated ion channels in health and disease. *Nat Rev Mol Cell Biol*. 2017;18(12):771-783.

3. Beech DJ, Kalli AC. Force Sensing by PIEZO Channels in Cardiovascular Health and Disease. *Arterioscler Thromb Vasc Biol*. 2019; 39(11):2228-2239.

4. Wu J, Lewis AH, Grandl J. Touch, Tension, and Transduction – The Function and Regulation of PIEZO Ion Channels. *Trends in Biochemical Sciences*. 2017;42(1):57-71.

5. Zarychanski R, Schulz VP, Houston BL, et al. Mutations in the mechanotransduction protein PIEZO1 are associated with hereditary xerocytosis. *Blood*. 2012;120(9):1908-1915.

6. Andolfo I, Alper SL, De Franceschi L, et al. Multiple clinical forms of dehydrated hereditary stomatocytosis arise from mutations in PIEZO1. *Blood*. 2013;121(19):3925.

7. Albuisson J, Murthy SE, Bandell M, et al. Dehydrated hereditary stomatocytosis linked to gain-of-function mutations in mechanically activated PIEZO1 ion channels. *Nat Commun*. 2013;4:1884.

8. Bae C, Gnanasambandam R, Nicolai C, Sachs F, Gottlieb PA. Xerocytosis is caused by mutations that alter the kinetics of the mechanosensitive channel PIEZO1. *Proceedings of the National Academy of Sciences*. 2013;110(12):E1162-E1168.

9. Glogowska E, Schneider ER, Maksimova Y, et al. Novel mechanisms of PIEZO1 dysfunction in hereditary xerocytosis. *Blood*. 2017;130(16):1845.

10. Shmukler BE, Vandorpe DH, Rivera A, Auerbach M, Brugnara C, Alper SL. Dehydrated stomatocytic anemia due to the heterozygous mutation R2456H in the mechanosensitive cation channel PIEZO1: a case report. *Blood Cells, Molecules, and Diseases*. 2014;52(1):53-54.

11. Del Orbe Barreto R, Arrizabalaga B, De la Hoz Rastrollo AB, et al. Hereditary xerocytosis, a misleading anemia. *Ann Hematol*. 2016;95(9):1545-1546.

12. Gnanasambandam R, Rivera A, Vandorpe DH, et al. Increased Red Cell KCNN4 Activity in Sporadic Hereditary Xerocytosis Associated With Enhanced Single Channel Pressure Sensitivity of PIEZO1 Mutant V598M. *Hemasphere*. 2018;2(5):e55.

13. Iolascon A, Andolfo I, Russo R. Advances in understanding the pathogenesis of red cell membrane disorders. *British Journal of Haematology*. 2019;0(0).

14. Carella M, Stewart G, Ajetunmobi JF, et al. Genomewide Search for Dehydrated Hereditary Stomatocytosis (Hereditary Xerocytosis): Mapping of Locus to Chromosome 16 (16q23-qter). *The American Journal of Human Genetics*. 1998;63(3):810-816.

15. Rotordam MG, Fermo E, Becker N, et al. A novel gain-of-function mutation of PIEZO1 is functionally affirmed in red blood cells by high-throughput patch clamp. *Haematologica*. 2019;104(5):e179-e183.

16. Ma Y, Zhao Y, Cai Z, Hao X. Mutations in PIEZO2 contribute to Gordon syndrome, Marden-Walker syndrome and distal arthrogryposis: A bioinformatics analysis of mechanisms. *Experimental and Therapeutic Medicine*. 2019;17(5):3518-3524.

17. Cahalan SM, Lukacs V, Ranade SS, Chien S, Bandell M, Patapoutian A. PIEZO1 links mechanical forces to red blood cell volume. *Elife*. 2015;4.

18. Ma S, Cahalan S, LaMonte G, et al. Common PIEZO1 Allele in African Populations Causes RBC Dehydration and Attenuates Plasmodium Infection. *Cell*. 2018;173(2):443-455 e412.

19. Rapetti-Mauss R, Picard V, Guitton C, et al. Red blood cell Gardos channel (KCNN4):the essential determinant of erythrocyte dehydration in Hereditary Xerocytosis. *Haematologica*. 2017: 102(10):e415-e418.

20. Kaestner L, Bogdanova A, Egee S. Calcium Channels and Calcium-Regulated Channels in Human Red Blood Cells. *Adv Exp Med Biol*. 2020;1131:625-648.

21. Rode B, Shi J, Endesh N, et al. PIEZO1 channels sense whole body physical activity to reset cardiovascular homeostasis and enhance performance. *Nature Commun*. 2017;8(1):350.

22. Bae C, Sachs F, Gottlieb PA. The mechanosensitive ion channel PIEZO1 is inhibited by the peptide GsMTx4. *Biochemistry*. 2011;50(29):6295-6300.

23. Shi J, Hyman AJ, De Vecchis D, et al. Sphingomyelinase disables PIEZO1 channel inactivation to enable sustained response to mechanical force. *bioRxiv*. 2019;792564(https://doi.org/10.1101/792564).

24. Abed M, Towhid ST, Mia S, et al. Sphingomyelinase-induced adhesion of eryptotic erythrocytes to endothelial cells. *Am J Physiol Cell Physiol*. 2012;303(9):C991-999.

25. Dinkla S, Wessels K, Verdurmen WP, et al. Functional consequences of sphingomyelinase-induced changes in erythrocyte membrane structure. *Cell Death Dis*. 2012;3:e410.

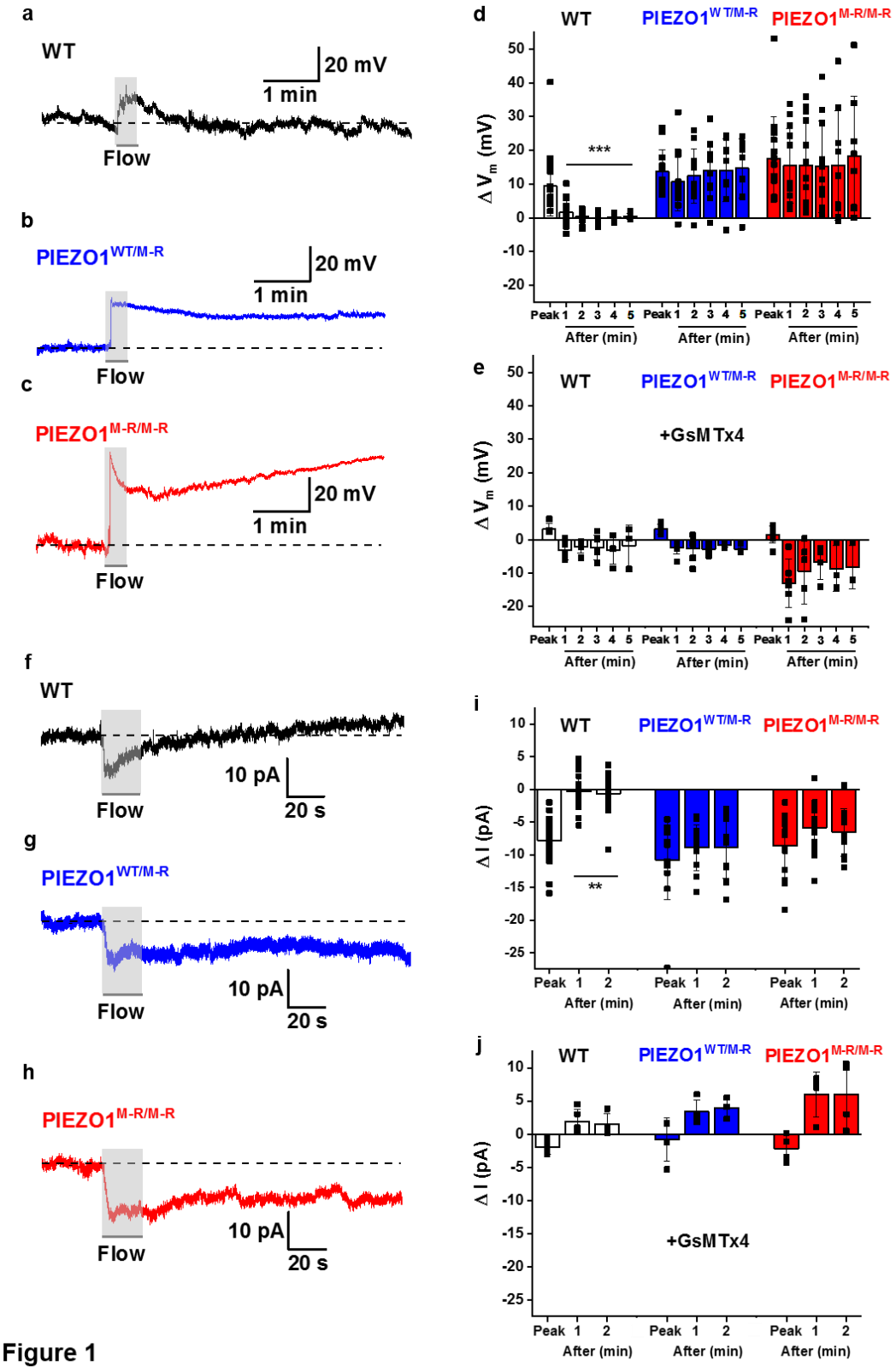

Figure 1

Figure 1. Slow kinetics of RBC PIEZO1 and slow recovery of PIEZO1$^{WT/M-R}$ and PIEZO1$^{M-R/M-R}$. (**a-c**) Membrane potential (V_m) recordings obtained using perforated-patch whole-cell mode applied to freshly-isolated RBCs from wildtype (WT) (**a**), PIEZO1$^{WT/M-R}$ (**b**) or PIEZO1$^{M-R/M-R}$ mice (**c**). RBCs were exposed to 20 µL.s^{-1} fluid flow for 20 s as indicated by the shaded areas. (**d**) Summary data for experiments of the type shown in (**a-c**). Presented is the peak (maximum) change in V_m of WT,

PIEZO1$^{WT/M-R}$ and PIEZO1$^{M-R/M-R}$ RBCs after exposure to flow and then the V_m at 1-5 min after flow. Averaged data are displayed as mean ± s.d. and each individual data point is shown. WT: n = 20 (max, 1 min), 16 (2 min), 13 (3 min), 9 (4 and 5 min); PIEZO1$^{WT/M-R}$: n = 13 (max), 12 (1 min), 11 (2 min), 10 (3 min), 9 (4 and 5 min); PIEZO1$^{M-R/M-R}$: n = 14 (max, 1 min), 13 (2 min), 11 (3 min), 9 (4 min), 8 (5 min). (**e**) As for (**d**) except with 2.5 μM GsMTx4 in the extracellular solution. WT: n = 5 (max, 1 min, 2 min, 3 min), 4 (4 min), 3 (5 min); PIEZO1$^{WT/M-R}$: n = 7 (max, 1 min), 6 (2 min), 4 (3 and 4 min), 3 (5 min); PIEZO1$^{M-R/M-R}$: n = 8 (max), 6 (1 min), 5 (2 min), 4 (3 min), 3 (4 and 5 min). (**f-h**) Ionic current recordings obtained using perforated-patch technique in whole-cell voltage-clamp mode applied to freshly-isolated RBCs from wildtype (WT) (**f**), PIEZO1$^{WT/M-R}$ (**g**) or PIEZO1$^{M-R/M-R}$ mice (**h**). RBCs were exposed to 20 μL.s^{-1} fluid flow for 20 s as indicated by the shaded areas. Holding voltage was -80 mV. (**i**) Summary data for experiments of the type shown in (**f**-**h**). Presented is the peak (maximum) change in current (ΔI) of WT and PIEZO1$^{M-R/M-R}$ RBCs after exposure to flow and then the ΔI at 1 and 2 min after flow. Averaged data are displayed as mean ± s.d. and each individual data point is shown. WT: n = 23 (max, 1 min), 15 (2 min); PIEZO1$^{WT/M-R}$; n = 12 (max, 1 min), 10 (2 min); PIEZO1$^{M-R/M-R}$; n = 18 (max), 15 (1 min), 11 (2 min). (**j**) As for (**i**) except with 2.5 μM GsMTx4 in the extracellular solution. WT: n = 5 (max, 1 min, 2 min); PIEZO1$^{WT/M-R}$: n = 4 (max, 1 min), 3 (2 min); PIEZO1$^{M-R/M-R}$: n = 4 (max, 1 min, 2 min). Statistical analysis by one-way ANOVA with Bonferroni's post-hoc test indicated: (**d**, **i**) significant decay of the WT (P ** <0.01 or *** P < 0.001) but not mutant RBC responses; (**d**) significant increase of the Peak response in PIEZO1$^{M-R/M-R}$ RBCs compared with WT (P <0.05); (**e**) no significant effects of flow in WT or PIEZO1$^{WT/M-R}$ but significant hyperpolarisation at 1 min compared with Peak in PIEZO1$^{M-R/M-R}$ (P < 0.01); and (**j**) no significant effects of flow in WT or PIEZO1$^{WT/M-R}$ but significant outward current at 1 and 2 min compared with Peak in PIEZO1$^{M-R/M-R}$ (P < 0.001).

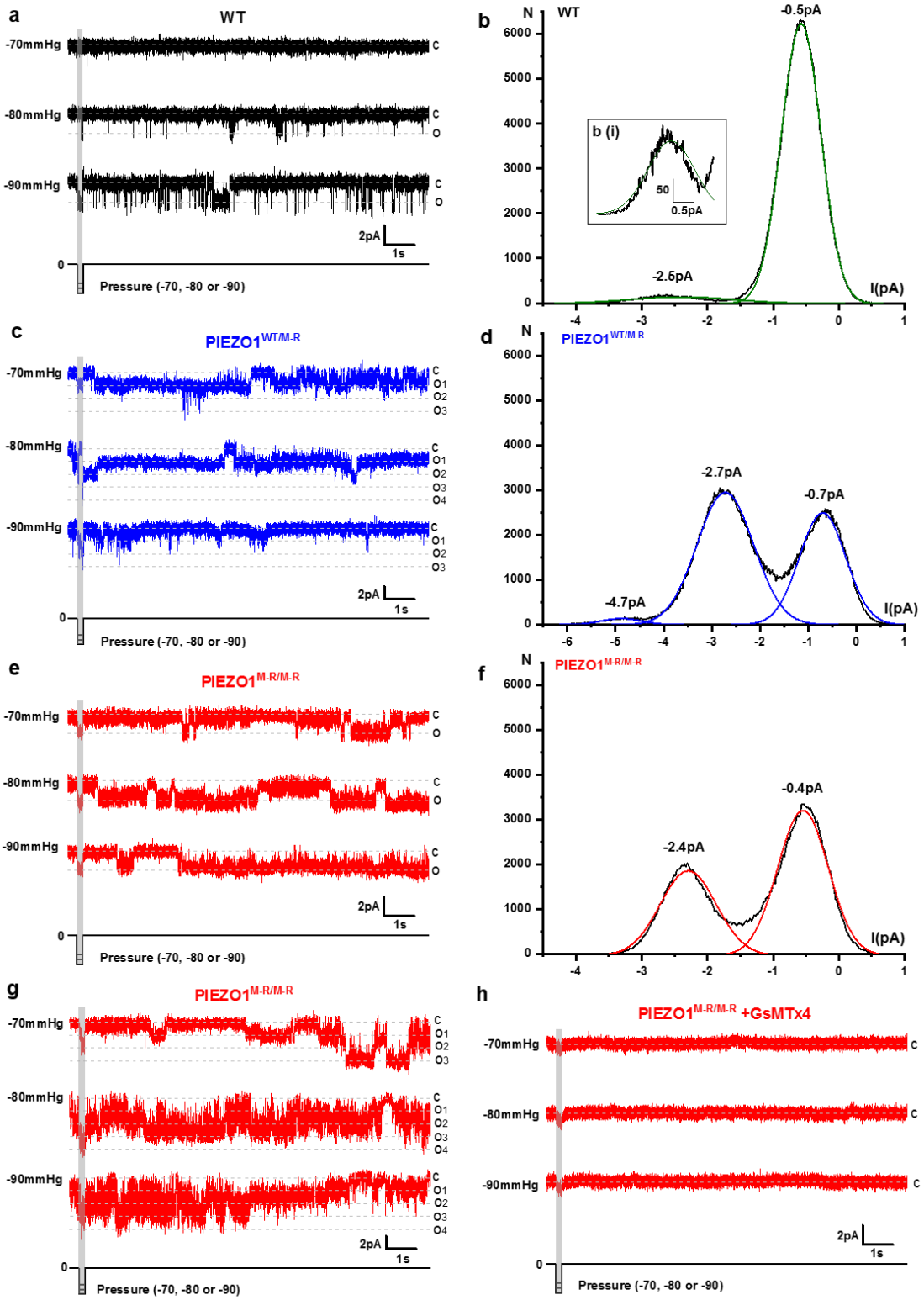

Figure 2. Failure of deactivation in PIEZO1$^{WT/M-R}$ and PIEZO1$^{M-R/M-R}$ single channels. Data are for single channel activity measured by cell-attached patch technique applied to freshly-isolated RBCs of wildtype (WT) mice (**a**, **b**), PIEZO1$^{WT/M-R}$ mice (**c**, **d**) and PIEZO1$^{M-R/M-R}$ mice (**e-h**). A fast pressure-

clamp system applied brief (200-ms) negative pressure pulses to the patches as indicated below the original exemplar current traces (**a**, **c**, **e**, **g**, **h**). Dashed horizontal lines indicate current levels for closed channels (C) and open channels (O, or O1-4 for multiple channel openings in **c** and **g**). Constant voltage of +80 mV was applied to the patch pipette. Data in (**a**) and (**e**) are considered to be for patches each containing only 1 PIEZO1 channel, whereas the patches in (**c**) and (**g**) contained multiple PIEZO1 channels. (**b**, **d**, **f**) Amplitude histogram analysis for the exemplar traces, showing plots of the frequency of detection of events (N) at the current amplitudes indicated on the x-axis, where zero current indicates no current flowing in the circuit. The closed channel state appears as a small negative current peaking at -0.5, -0.7 and -0.4 pA in (**b**), (**d**) and (**f**) respectively. The small amount of open channel activity at -2.5 pA in (**b**) is shown expanded in the inset panel (**b (i)**). Raw data are shown with superimposed Gaussian fits in green (WT), blue ($PIEZO1^{WT/M\text{-}R}$) and red ($PIEZO1^{M\text{-}R/M\text{-}R}$). Representative of n = 6, n = 5 and n = 4 for WT, $PIEZO1^{WT/M\text{-}R}$ and $PIEZO1^{M\text{-}R/M\text{-}R}$ respectively. (**h**) An exemplar recording from a $PIEZO1^{M\text{-}R/M\text{-}R}$ RBC patch with 2.5 μM GsMTx4 in the extracellular solution. Representative of n = 5.

SUPPLEMENTAL INFORMATION (SI)

RBCs prevent rapid PIEZO1 inactivation and expose slow deactivation as a mechanism of DHS

Elizabeth L Evans[†1], Oleksandr V Povstyan[†1], Dario De Vecchis[1], Fraser Macrae[1], Laeticia Lichtenstein[1], T Simon Futers[1], Gregory Parsonage[1], Neil Humphreys[2], Antony Adamson[2], Antreas C Kalli*[1], Melanie J Ludlow*[1], David J Beech*[1]

[1]School of Medicine, University of Leeds, Leeds, England, UK. [2]Faculty of Biology, Medicine and Health, University of Manchester, AV Hill Building, Manchester M13 9PT, UK

[†]Equal contributors

*Authors for correspondence: Professor David Beech, Leeds Institute of Cardiovascular and Metabolic Medicine, School of Medicine, LIGHT Building, Clarendon Way, University of Leeds, Leeds LS2 9JT, UK. Email d.j.beech@leeds.ac.uk. Dr Melanie Ludlow, Leeds Institute of Cardiovascular and Metabolic Medicine, School of Medicine, LIGHT Building, Clarendon Way, University of Leeds, Leeds LS2 9JT, UK. Email m.j.ludlow@leeds.ac.uk. Dr Antreas Kalli, Leeds Institute of Cardiovascular and Metabolic Medicine, LIGHT Building, Clarendon Way, School of Medicine, University of Leeds, Leeds LS2 9JT, UK. E-mail a.kalli@leeds.ac.uk. Telephone +44 (0) 0113 343 7722.

SUPPLEMENTAL RESULTS

Mouse PIEZO1 channel is similar to human PIEZO1 channel Missing unstructured regions were modelled in the 3D structure of the mouse PIEZO1 channel derived by electron microscopy[1] and then a homology model of the human channel was generated based on the mouse PIEZO1 structure (Figure S1a). The channels were similar (Figure S1a). M2225 is situated in the C-terminal Extracellular Domain (CED), as indicated by the black dashed boxes in Figure S1a. Overlay of the human and mouse channels at this position showed that the channels were almost identical around M2225 (Figure S1b). Moreover, the position of the mouse equivalent of M2225R (M2241R) and its nearby residues suggested no obvious difference from the human situation (Figure S1b). For contrast, the mouse model is also shown for alanine (M2241A) in place of arginine (M2241R). The modelled structures suggest suitability of mouse PIEZO1 for understanding the human channel.

Overexpressed mutant mouse PIEZO1 exhibits gain-of-function To further test the suitability of the mouse channel we looked for gain-of-function by generating the mutation in mouse PIEZO1 clone and overexpressing it in a cell line. A functional test was performed by measuring the intracellular Ca^{2+} concentration and applying the PIEZO1 channel agonist, Yoda1 (Figure S2). M2241R approximately doubled the response to 0.3 μM Yoda1 and increased the response to 1 μM Yoda1 by about 60 % (Figure S2). Studies of artificial mutations at position 2241 suggested that it was the switch to a positive charge that caused the gain-of-function because mutation to lysine (M2241K) conferred similar increase in the Yoda1 response whereas mutation to alanine (M2241A) or glutamic acid (M2241E) failed to enhance the response (Figure S2). The data further support use of the mouse channel in understanding the impact of the human mutation M2225R.

M2241R mice display features of DHS A mutant mouse was generated in which M2241R occurred in the endogenous PIEZO1 channel (Figures S3 and S4). We first studied mice that were homozygote for the mutation ($PIEZO1^{M\text{-}R/M\text{-}R}$ mice) at 8 weeks old. These mice exhibited stomatocytes, which is an expected feature of DHS (Figure S5). They also showed reduced osmotic fragility (Figure S6). Mice that were heterozygote for the mutation ($PIEZO1^{WT/M\text{-}R}$) had milder but nevertheless significantly reduced osmotic fragility (Figure S6). At 8 weeks old, $PIEZO1^{M\text{-}R/M\text{-}R}$ mice showed a trend towards increased weight of the spleen, but it failed to reach statistical significance (Figure S7a). At 22 weeks

of age, significant increase in the weight of the spleen became apparent (Figure S7b). PIEZO1$^{WT/M-R}$ mice showed the expected Mendelian live-birth ratio of 2:1 compared with wildtype (WT) but there were slightly fewer than expected PIEZO1$^{M-R/M-R}$ live births, suggesting a possible negative effect of homozygosity (Figure S8a). Comparison of body weight increase in adult WT and PIEZO1$^{M-R/M-R}$ mice between 21 and 56 days of age revealed no difference (Figure S8b). Haematological analysis of 8 week-old PIEZO1$^{M-R/M-R}$ mice revealed some of the expected features of DHS[2] (Table S1) as described in the main Letter. Liver function tests revealed no difference (Table S2). Iron and total iron binding capacity were not significantly different but there appeared to be trends towards increases in these parameters. A sensitive transferrin assay revealed a small significant increase in transferrin (Table S2). The data suggest that M2241R recapitulates key features of DHS but that there may be age-dependent effects, such that studies of older M2241R mice could reveal differences not yet evident in 8 week-old mice.

Resting membrane potential of mutant RBCs is slightly hyperpolarised The resting membrane potential of PIEZO1$^{M-R/M-R}$ RBCs was slightly hyperpolarised compared to WT RBCs (mean ± s.d.) at -9.8 ± 2.4 mV (n=18, PIEZO1$^{M-R/M-R}$) compared with -7.5 ± 2.3 mV (n=17, WT) ($P < 0.01$). PIEZO1$^{WT/M-R}$ RBCs were intermediate at -8.0 ± 1.5 mV (n=16) ($P = 0.052$ compared with PIEZO1$^{M-R/M-R}$). Statistical analysis used one-way ANOVA with Bonferroni's post-hoc test.

Wash-out of GsMTx4 reveals wildtype-like properties of mutant RBCs. As indicated in the main Letter, wash-out of GsMTx4 from mutant RBCs revealed recover to a type of activity that was more like the activity of wildtype RBCs in the absence of toxin, suggesting the potential to correct the mutant channel behaviour. The supporting data firstly show the exemplar traces for inhibition of the flow-evoked depolarisation in the presence of 2.5 μM GsMTx4 (Supplemental Figure S9a-c), the mean data for which are presented in Figure 1e. It is apparent that the depolarisation was not only prevented by GsMTx4 but that a hyperpolarisation was revealed, especially in PIEZO1$^{M-R/M-R}$ RBCs. The hyperpolarisation was slower in onset (e.g. Figure S9c) compared with the depolarisation in the absence of GsMTx4 (e.g. Figure 1c) and we suggest that this effect was most likely mediated by other ionic mechanisms. We studied the effect of washing out GsMTx4 on PIEZO1$^{WT/M-R}$ and PIEZO1$^{M-R/M-R}$ RBCs because pilot studies indicated an intriguing response: After wash-out, the flow response of mutant RBCs resembled the response of wildtype RBCs in the absence of GsMTx4 because there was depolarisation that recovered back to baseline after flow stopped (Figure S9d-f *cf* Figure 1a, d). Similar but even more striking observations were made when membrane current was recorded under voltage-clamp (Figure S10). GsMTx4 caused the flow response to reverse in polarity, becoming an outward current, which was slow to occur and especially obvious after flow had stopped (Figure 1j and Figure S10a-c). After wash-out of GsMTx4, flow caused inward current that relaxed back to baseline after flow stopped (Figure S10d-f), similar to observations for wildtype RBCs in the absence of GsMTx4 (Figure 1f, i). The data suggest the possibility to pharmacologically revert mutant channel activity back to wildtype-like behaviour.

Channel conductance Unitary current was measured for a range of voltages to generate I-V relationships for PIEZO1$^{WT/M-R}$ RBCs. The I-Vs were linear and the indicated unitary conductance was 25.3 pS, which is expected for PIEZO1 channels (Figure S11).

Multi-channel activity analysis Activity of multi-channel patches was analysed by measuring NP_o after application of a range of pressure pulses for wildtype, PIEZO1$^{WT/M-R}$ and PIEZO1$^{M-R/M-R}$ RBCs, as shown in the exemplar traces of Figure 2. From these data it is apparent that wildtype channels were largely closed after the pressure pulse ceased, whereas mutant channels retained activity (Figure S12). In the absence of applied pressure, NP_o was 0.0079 ± 0.0106 for wildtype (n=6), 0.0100 ± 0.0189 for PIEZO1$^{WT/M-R}$ (n=5) and 0.0206 ± 0.0179 for PIEZO1$^{M-R/M-R}$ (n=3). The maximum pressure-evoked NP_o values were 0.1626 ± 0.2017 for wildtype (n=6), 0.7315 ± 1.0806 for PIEZO1$^{WT/M-R}$ (n=5) and 1.0305 ± 0.3489 for PIEZO1$^{M-R/M-R}$ (n=3). Although the data showed considerable variability, the suggestion is that the heterozygotes were intermediate between wildtype and homozygote.

SUPPLEMENTAL DISCUSSION

Key points arising from this study are that: RBCs disable the rapid PIEZO1 inactivation seen in overexpression systems to reveal slower gating that is compatible with physiology; RBC PIEZO1 is activated by fluid flow; and the murine equivalent of the M2225R DHS mutation causes PIEZO1 hyperactivity (gain-of-function) by disrupting deactivation.

Inactivation and deactivation are distinct mechanisms: Inactivation is a type of desensitisation - channel closure despite continuous presence of the activation stimulus; while deactivation does not occur during continuous stimulation but only when the activation stimulus is removed. Some ion channels exhibit no inactivation, yet they still deactivate. Some are dominated by inactivation but are still capable of deactivation. A common important characteristic of inactivation is the depth of its associated closed state, which can result in slow recovery from inactivation and thus refractory periods that affect the frequency of events such as action potential firing. We know relatively little about the molecular mechanisms of inactivation and deactivation in PIEZO1 channels, but amino acid residues contributing to rapid inactivation have been suggested[3] and our molecular dynamics simulations of PIEZO1 indicate how activation might occur[4]; opening the way to deactivation studies. Our data suggest that priorities for future PIEZO1 and PIEZO1-related DHS studies in RBCs should be the determination of how the rapid inactivation mechanism is disabled and how deactivation occurs at the molecular level. We studied only M2225R/M2241R, so it will be interesting to investigate other PIEZO1-related DHS mutations in the native RBC to see if deactivation is also relevant.

Prior work indicated the mechanism of action of M2225R to be a subtle but significant slowing of the rate of rapid inactivation[5-7] but our data suggest that such a rapid process (time constant ~10-ms) may not be physiologically relevant. We conclude that RBCs disable this rapid inactivation to reveal a much slower type of inactivation (at least 2 orders of magnitude slower) or that they greatly slow the rapid inactivation gate. We do not exclude importance of changes in inactivation in DHS because we observed very slow inactivation and M2241R slowed it further or abolished it, but M2241R-induced changes in deactivation were more striking. The removal of rapid inactivation exposes the additional deactivation feature. Disrupted deactivation theoretically creates a gain-of-function imbalance in which there is too much activation (opening) relative to deactivation (closing). Prior studies suggest that the threshold and rate of mechanical activation in M2225R is approximately the same as wildtype (i.e., suggesting no change in activation[6,7]) and our observations are consistent with this conclusion (Figure 1f-i). Therefore, an imbalance of activation/deactivation is likely and could cause problems for RBCs both in constant fluid flow and when flow is altered or stopped, as might occur for example in the spleen, vascular junctions with disturbed flow, a thrombus or a blood storage container.

We consider it likely that RBC PIEZO1 channels sense fluid flow relatively directly. This suggestion is based primarily on studies of PIEZO1 in other cell types. In endothelium, where PIEZO1 is also functional, we observed robust PIEZO1 activation by fluid flow in excised membrane patches, suggesting a close relationship between PIEZO1 and flow[8]. In addition, by introducing exogenous PIEZO1, it has been possible to reconstitute fluid flow responses in HEK 293 cells that are otherwise resistant to fluid flow[9-11]. There is also independent evidence that PIEZO1 can be mechanically activated after reconstitution in an artificial lipid bilayer[12] and that it curves the bilayer[1]. Nevertheless, it would be premature to conclude that PIEZO1 channels are directly activated by fluid flow in native systems such as RBCs because the flow may act via the lipid bilayer or other unknown proteins closely associated with PIEZO1. Indeed, we have noted previously that Ca^{2+} entry responses are not reliably reconstituted by PIEZO1 in all batches of HEK 293 cells and that this could potentially be explained by different batches of HEK 293 cells containing different amounts of a putative cofactor[13].

How M2225R/M2241R acts at the molecular level remains unknown. The mutation is in the C-terminal Extracellular Domain (CED) and so it is not immediately obvious how this might affect gating at the ion pore. But it is known that the CED has feet-like projections that make contact with the membrane-spanning domains close to the ion pore region[1]. Therefore, conformation of CED may determine how

it interacts with the main body of PIEZO1 such that mutations affecting the dynamic structure of CED stabilise or destabilise the interaction and thus ion channel activity. Our data suggest that the switch to a positively charged amino acid residue is critical in conferring gain-of-function. A potential explanation is the formation of *de novo* inter- or intra-subunit salt bridges. Two acidic amino acid residues are close in the structure (E2236 and E2287 in mouse PIEZO1) and could enable a salt bridge effect. Our Yoda1-response data suggest that M2241A and M2241E do not confer gain-of-function. The data are consistent with a positive charge at this position (M2241R) enabling a salt bridge to form. Methionine (M), alanine (A) and glutamate (E) would not be compatible with such a bridge. This hypothesis would ideally be tested further in the overexpression system and through studies of mechanical activation of the endogenous channel.

Overexpression techniques have led to the important conclusion that PIEZO1 forms mechanically-activated channels[14-16] and there is no reason to doubt this conclusion. Studies of native channels also suggest that PIEZO1 forms mechanically-activated channels, including those shown here and previously reported by us[8,9] and other groups[17-19]. Therefore, overexpression studies have been, and remain, useful. However, it is emerging from studies of other non-RBC cells types that native environments profoundly alter PIEZO1 properties and particularly the extent of inactivation and its kinetics[8,9,17,18,20,21]. The relevant factors in native cells could include PIEZO1 density (i.e., PIEZO1 channels affecting each other through proximity), local lipid constituents and associated protein factors such as cytoskeleton and other membrane proteins. Such factors might help explain why *PIEZO1* mutations associated with DHS apparently lead to such a restricted disease (i.e. only anaemia) when the gene is known to be widely expressed and functionally important[14,16,22].

GsMTx4 blocked the whole-cell depolarisation and inward current evoked by fluid flow and the single channel events activated by pressure pulses, consistent with them being mediated by PIEZO1 channels in both wildtype and mutant RBCs. GsMTx4 is not specific for PIEZO1 but does inhibit PIEZO1 channels at the concentration we used[23]. It was notable that the responses in RBCs were sometimes reversed in polarity in the presence of GsMTx4. This could be explained if the mechanical stimulus also activates another ionic mechanism that opposes, but which is normally obscured by, the PIEZO1 response. Further studies would be required to determine the identity of this mechanism. Previous studies have suggested that other channels are activated by fluid flow in RBCs[24,25].

We found that wash-out of GsMTx4 allowed recovery of activity and we prioritised study of these recovered responses in mutant RBCs. Intriguingly, the response became like that of wildtype RBCs in the absence of GsMTx4; i.e., there was deactivation, contrasting with the failed deactivation of mutant RBCs that are GsMTx4-naive. This suggests the possibility to pharmacologically revert mutant PIEZO1 channels to wildtype behaviour.

The exemplar pressure pulse data in Figure 2a show that relatively high pressure steps were sometimes needed to activate wildtype RBC PIEZO1 channels. However, in other patches we observed wildtype channels activated at -20 or -30 mmHg. These other data are not illustrated here but the whole-cell current data of Figure 1f-i do not suggest anything particularly different about the activation of wildtype and mutant channels. Single channel recordings necessarily display more variability than whole-cell recordings because of the smaller number of contributing unitary events. Large numbers of recordings would be needed to provide accurate estimates of pressure-activation curves from single channel data.

Considerable variability occurs in the phenotype of DHS patients and it will be interesting to explore such phenotypes in detail in M2241R mice. Here the primary aim was determination of native channel gating principles. In terms of phenotyping we sought only indications of whether the mutant mice displayed some of the expected DHS characteristics. In part they matched the patient data, but in other regards they did not. However, we are cautious in the interpretation at this stage and do not overstress differences because most of our measurements were made in young adult mice, mostly at 8 weeks of age. We found that the spleen weight was unaffected at 8 weeks but increased at 22 weeks of age. This suggests that the exact phenotype may depend on age, and perhaps other factors such as environmental factors and diet. One expected phenotype is iron overload, reflecting abnormal iron homeostasis or

disturbed RBC development. At the 8-week time point, iron concentration and total iron-binding capacity (TIBC) were not significantly affected in M2241R mutant mice. It will be worth investigating if there are differences when the mice are older, consistent with prior work suggesting age-related changes in ferritin[26]. Pseudohyperkalemia with or without hematologic abnormalities is also observed in some patients, so this should also be investigated as the mice become older. Until such data are available it would be premature to make a detailed evaluation of the mutant mice as a model of the human disease.

It is expected that individuals who are heterozygous for M2225R will have milder symptoms than individuals who are homozygous, and this was suggested in the initial discovery of this mutation[27]. However, the information available on these patients is relatively little and it would be premature to make a detail comparison of our observations on mice with patient data. Our data suggest that heterozygosity should cause intermediate phenotype, although the strength of the effect of heterozygosity on channel activity was impressive and close to homozygosity in many recordings, consistent with the view that heterozygosity is sufficient to cause DHS.

The effects we observed could potentially be relevant to malarial resistance because a prior study suggested that the gain-of-function mutations R2482H in mouse (R2456H in DHS patients) and E756del (in as much as a third of African populations) may protect against malaria[28]. To the best of our knowledge this remains to be investigated for M2225R. Unexpectedly a subsequent study found no effect of E756del on RBC phenotype[29], so further studies are needed to clarify the impact of this mutation. In overexpression experiments, E756del approximately doubled the amplitude of the response to high concentrations of Yoda1 but the effect on rapid inactivation was relatively small, although statistically significant[28]. It will be interesting to determine the effect of E756del on the electrophysiological properties of native PIEZO1 and its response to fluid flow.

Our successful generation of a second mouse model of DHS (the first for M2225R) should be useful for further understanding DHS and developing therapeutic strategies to combat it. The first-published mouse model addressed the R2482H mutation[28]. Small-molecule activators of PIEZO1 are effective at mouse and human RBCs[30,31] and could be tested in wildtype mice to see if malarial resistance can be achieved. Activators might also be useful in cases of loss-of-function *PIEZO1* mutations that have been associated with non-immune hydrops fetalis and Generalised Lymphatic Dysplasia[32,33]. The available activator, Yoda1, exhibits relatively modest aqueous solubility[34] and limited suitability for many in vivo applications and so should be considered as a tool compound for use only in specific situations. However, medicinal chemistry refinement of Yoda1 has been initiated[35] and new activators may be discovered, paving the way for in vivo testing. If PIEZO1 inhibitors are discovered, they might be tested in M2241R mice for potential protection against anaemia because our GsMTx4 wash-out data suggest the possibility for correction of abnormal deactivation. The apparent external accessibility of M2225R/M2241R in the CED suggests that small-molecules or other agents could potentially be designed to interact with the site and thereby modulate or correct the defect.

METHODS

Murine PIEZO1 channel model Structural data were obtained from the mouse cryo-EM structure PDB: 6B3R[1]. Missing residues were added with MODELLER (v 9.19)[36] and the loop refinement tool[37] was used to remove a knot in one chain between residues 1490-1498. The best loop was selected out of 10 candidates according to the discrete optimized protein energy (DOPE) method[38]. The final PIEZO1 mouse model does not comprises the first N-terminal 576 residues and residues 718-781, 1366-1492, 1579-1654, 1808-1951. Therefore, each chain is composed by five non-overlapping fragments: residues 577-717, 782-1365, 1493-1578, 1655-1807 and 1952-2547. The model obtained was further energy minimized in vacuum with GROMACS 5.0.7[39] and the CHARMM36 force field[40].

Human PIEZO1 channel model The human PIEZO1 protein sequence was obtained from the UniProtKB database (Universal Protein Resource Knowledgebase)[41]. The T-coffee method[42] was used to obtain the final target-template alignment between the human and the mouse PIEZO1 sequences and

used in conjunction with MODELLER (v 9.19)[36] to generate the initial human model. Unstructured residues 595-598, 881-884, 892-896, 1982-1998 and 2050-2058 from the initial human model were refined using the loop refinement tool[37] from MODELLER and selecting the best loop out of 5 candidates according the DOPE method[38]. The model obtained was further energy minimized in vacuum with GROMACS 5.0.7[39] and the CHARMM36 force field[40].

Generation of the PIEZO1 model mutants and molecular graphics The Dunbrack rotamer library [43] implemented in UCSF Chimera (v 1.12)[44] was used to generate the PIEZO1 model mutants of the M2225 and the M2241, for human and mouse respectively. Molecular graphics were generated using UCSF Chimera (v 1.12)[44].

Generation of PIEZO1$^{M\text{-}R/M\text{-}R}$ mice Mice were generated using CRISPR/Cas9 methodology. The guide RNA (gRNA) was designed to direct Cas9-mediated cleavage of PIEZO1 6-bp upstream of the target methionine codon with no off-target sites of less than 3 mismatches predicted elsewhere in the genome (binding sequence 5' GGGCGCUCAUGGUGAACAG 3'). A 120 nucleotide single-stranded homology-directed repair (ssHDR) template was designed to incorporate the methionine to arginine missense mutation, in addition to silent mutations introducing a Mlu1 restriction enzyme recognition site to facilitate genotyping (5'ccacccgtcccctgagcctgaggggctccatg ctgagcgtgcttccatccccagccaTTAttTacGCGTagcgcccagcagccatccattgtgccattcacaccccaggcctacgaggag 3'; capital letters denote the mutated bases) (Sigma Aldrich). The gRNA, delivered as an alt-R crRNA combined with tracrRNA (Integrated DNA Technologies, Illnois, USA), Cas9 protein (New England Biolabs) and PAGE purified ssHDR template (Integrated DNA Technologies, Illnois, USA) were microinjected into C57BL/6 mouse zygotes and implanted in females (University of Manchester Transgenic unit). Successful gene editing of pups was identified by Mlu1 digestion of PCR amplicons (F: 5' TCTGGTTCCCTCTGCTCTTC 3', R: 5' TGCCTTCGTGCCGTACTG 3') and confirmed by DNA sequencing following sub-cloning into pCRTM-Blunt (Invitrogen). Further genotypes were determined by real-time PCR with specific probes designed for each gene (Transnetyx, Cordova, TN). All animal experiments were authorised by the University of Leeds Animal Ethics Committee and UK Home Office. Mice were housed in GM500 individually ventilated cages (Animal Care Systems) at 21 °C, 50-70% humidity with a 12-hr alternating light/dark cycle. They had *ad libitum* access to RM1 diet (SpecialDiet Services) with bedding from Pure'o Cell (Datesand). Eight week-old male mice were used for experiments unless otherwise stated.

Generation of PIEZO1 M2241 mutants Mouse PIEZO1 cDNA was cloned as described[21]. mPIEZO1 mutants were made using site-directed mutagenesis using primers as follows: M2241R (F: CCACTGTTCACCAGGAGCGCCCAGCAG; R: CTGCTGGGCGCTCCTGGTGAACAGTGG). M2241K (F: GCCACTGTTCACCAAGAGCGCCCAGCAGC; R: GCTGCTGGGCGCTCTTGGTGAACAGTGGC). M2241A (F: GAGCCACTGTTCACCGCGAGCGCCCAGCAG; R: CTGCTGGGCGCTCGCGGTGAACAGTGGCTC). M2241E (F: GAGCCACTGTTCACCGAGAGCGCCCAGCAGC; R: GCTGCTGGGCGCTCTCGGTGAACAGTGGCTC). HEK-293 cells (Invitrogen) were transfected with 1 µg pcDNA4/TO-mPIEZO1/mPIEZO1M2241X (X: R, K, A or E) using Lipofectamine 2000 (Invitrogen), 48 h prior to experiments. HEK-293 cells were maintained in DMEM supplemented with 10% fetal calf serum and 1% penicillin/streptomycin (Sigma-Aldrich).

Intracellular Ca^{2+} measurements HEK 293 cells were plated in poly-d-lysine coated 96-well plates (Corning, NY, USA) at a confluence of 90%, 24 h before experimentation. Cells were incubated with 2 µM fura-2-AM (Molecular Probes™) in the presence of 0.01% pluronic acid (Thermo Fisher Scientific) in standard bath solution (SBS) for 1 h at 37 °C. Cells were washed with SBS for 30 min at room temperature. Measurements were made at room temperature on a 96-well fluorescence plate reader (FlexStation, Molecular Devices, Sunnyvale, CA, USA) controlled by Softmax Pro software v5.4.5. The change (Δ) in intracellular Ca^{2+} was indicated as the ratio of fura-2 emission (510 nm) intensities for 340 and 380 nm excitation. The SBS contained (mM): 130 NaCl, 5 KCl, 8 D-glucose, 10 HEPES, 1.2 $MgCl_2$, 1.5 $CaCl_2$ and the pH was titrated to 7.4 with NaOH.

RBC fragility and other blood analysis Blood was diluted 1:8 into saline containing 2mM HEPES (pH 7.4). 10 µl of this diluted blood was added to each well on a row of a 96-well U-bottomed plate (8 wells per sample). 225 µl tonicity solutions were added containing saline at concentrations of 0, 20, 25, 30, 35, 40, 45, 50, 55, 60, 80 and 100%, made up in water. The plate was left at room temperature for 5 min before centrifugation for 5 min at 1000xg. 150 µL of the supernatant was transferred into a well of a flat-bottomed 96-well clear plate. The absorbance was measured at 540 nm using a FlexStation (Molecular Devices). Haemotological properties of the mice were analysed by The Blood Sciences Laboratory, Leeds Teaching Hospitals, Leeds, UK. Full blood and reticulocyte counts were analysed by an ADVIA 2120i Haematology System. Samples were only analysed if hemolytic indices were 0 or +. Hemolysis indices were measured by Advia Chemistry XPT system. Border values were: 0 = 0 - 0.04 g/dL; + = 0.05 - 0.13 g/dL; ++ = 0.14 - 0.23 g/dL; +++ = 0.24 - 0.44 g/dL; ++++ >= 0.45 g/dL. Blood smears were stained with May-Grunwald followed by Giesma and imaged by a Nikon Eclipse E400 light microscope, fitted with a Nikon Digital Camera DXM1200. Liver function tests were analysed using an ADVIA Chemistry XPT System.

Electron microscopy Clots for scanning electron microscopy (SEM) were prepared by adding 10 µL activation mixture (0.5 $U.mL^{-1}$ murine thrombin [Enzyme Research Laboratories], $CaCl_2$ 5 mM in phosphate-buffered saline (PBS, pH 7.4)) to 100 µL of whole blood. The clotting mixture was immediately transferred to pierced Eppendorf lids. Clots were left to form in a humidified chamber at room temperature for 2 hr. Clots were washed with saline solution to remove excess salt and prepared for microscopy by fixation in 2% glutaraldehyde solution for at least 2 hr. Clots were further washed with sodium cacodylate buffer (67 mM $C_2H_6AsNaO_2$, pH 7.4) and dehydrated in a series of increasing acetone concentrations (30%–100%). Clots were critical-point dried with CO_2, mounted onto stubs, and sputter coated with platinum using a Cressington 208 HR (Cressington Scientific Instruments). Each clot was formed in duplicate and imaged in 5 areas at different magnifications (5000×, 10000×) using a Hitachi SU8230 high-performance cold field emission (CFE) SEM (Chiyoda).

Isolation of RBCs for patch-clamp studies 500 µL whole blood was collected in EDTA tubes and centrifuged at 10000g for 10 min at 4 °C. Plasma was removed and RBCs were washed twice with 1 mL PBS followed by 1 min centrifugation under the same conditions. 2-µL of resulting haematocrit was resuspended in 5 mL PBS, plated onto borosilicate glass coverslips and left to settle for 30 min before recordings.

Patch-clamp recordings Experiments were conducted in standard perforated-patch whole-cell (current- and voltage-clamp modes) and cell-attached (voltage-clamp) configurations. All recordings were made using AXOpatch 200B amplifier (Axon Instruments, Inc., USA) equipped with Digidata 1550B hosted by a PC running pClamp 10.6 software (Molecular Devices, USA) at room temperature. Current records were analogue filtered at 2-5 kHz and digitally acquired at 5-20 kHz. Perforated-patch whole-cell transmembrane ionic currents were measured at a holding potential of −80 mV and cell-attached experiments were performed at a holding potential of +80 mV. RBCs were maintained during the experiment in an external solution of the following composition (mM): 135 NaCl, 4 KCl, 2 $CaCl_2$, 1 $MgCl_2$, 10 D-glucose and 10 HEPES (titrated to pH 7.4 with NaOH). 10 mM NaCl was equimolarly replaced with TEA-Cl in voltage-clamp experiments. Patch pipettes had a resistance of 20–25 MΩ when filled with pipette solution. The pipette solution for the perforated-patch whole-cell experiments contained (mM): 145 KCl, 1 $MgCl_2$, 0.5 EGTA, 10 HEPES (titrated to pH 7.2 with KOH) and was supplemented with freshly prepared amphotericin B (300 $\mu g.mL^{-1}$) before each experiment. For cell-attached experiments the pipettes were filled with TEA-containing external solution. For application of fluid flow, membrane patches were manoeuvred to the exit of a capillary tube with tip diameter of 350 µm, out of which ionic (bath) solution flowed at 20 $\mu l.s^{-1}$. In pressure-clamp experiments 200-ms pressure steps from 0 to -90 mmHg, with 10 mmHg increments, were applied directly to the patch pipette with an interval of 12 s using High Speed Pressure Clamp HSPC-1 System (ALA Scientific Instruments, USA). In current-clamp experiments the resting membrane potential of RBCs was measured for 20 s before manually hyperpolarisation to -80 mV by current injection. The fluid flow was applied approximately 1 min after the new potential had been established and become stable. The

membrane potential exhibited greater random fluctuations at -80 mV compared with the resting potential (Supplemental Figure S13). Single channel current amplitudes were calculated from idealized traces using the 50 % threshold method in pClamp 10.7 software. Channel activity was expressed as NP_o, as reported by pClamp 10.7 under Event Statistics following completion of the single-channel search procedure applied to idealized traces. Single-channel current amplitude histograms were plotted from the event data of the idealized traces with a 0.02 pA bin width. Amplitude histograms were fitted using Gaussian curves with peak values corresponding to channel open levels. Mean channel amplitudes at different membrane potentials were plotted and I–V relationships were fitted by linear regression with the gradient determining conductance value.

Mouse transferrin ELISA Blood was harvested from anaesthetised mice by cardiac puncture in a EDTA coated tube (1.3-ml EDTA K3, Sarstedt) and centrifuged at 4000 rpm for 10 min. Plasma was aliquoted and stored at -80 °C. ELISA measuring plasma levels of Transferrin (Abcam ab157724) was quantified according to the manufacturer's protocol. Assays were performed in duplicate and measured on microplate reader (FlexStation at 450nm).

Data analysis Averaged data are presented as mean ± standard deviation (s.d.). For comparisons between two sets of data, Student's t-tests were used. For multiple comparisons, one-way ANOVA was used with Bonferroni's post-hoc test. $P < 0.05$ was deemed significant (* <0.05, ** <0.01, *** <0.001). The genotypes of the mice were blinded to the experimental investigator. Data were analysed and plotted using pClamp 10.7 and Origin 2018 (OriginLab Corporation, USA). The letter n represents the number of independent biological experiments for a given result and is stated in the figure legends for each experiment. The number of independent repeats was at least 3. For multi-well plate assays, N is also indicated as the number of replicates within a single independent experiment.

SUPPLEMENTAL FIGURES

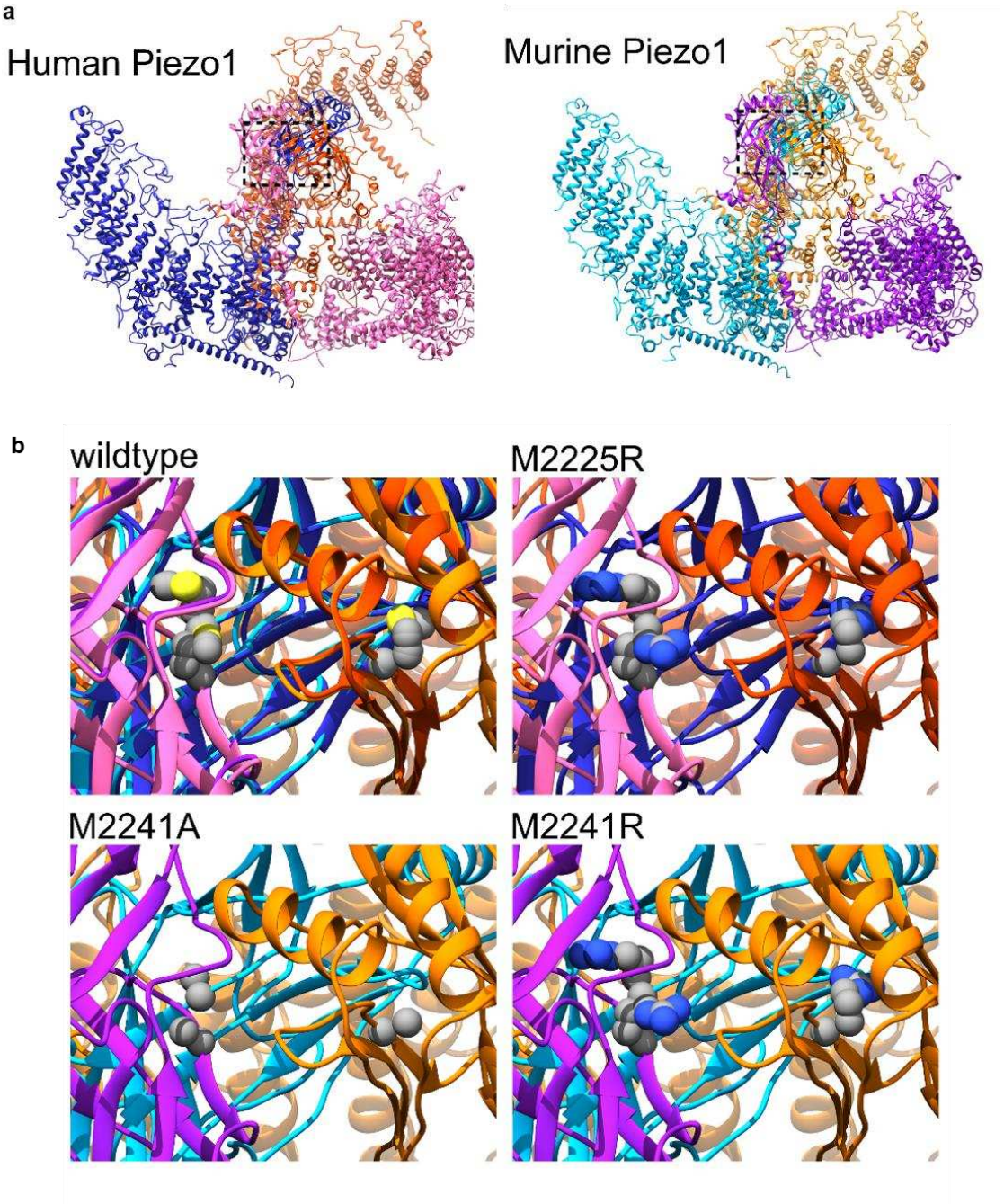

Figure S1. Mouse and human PIEZO1 are structurally similar. (**a**) Molecular models of human Piezo1 (left) and mouse Piezo1 (right). Each channel comprises three Piezo1 monomers, shown in different colors and ribbon representations (blue, orange, and pink for the human Piezo1 subunits; cyan, magenta, and light orange for the mouse Piezo1 subunits). The dashed black boxes indicate the regions of the C- terminal extracellular domain (CED) shown magnified in (**b**). (**b**) Each figure is a magnified view of all three Piezo1 monomers shown in (**a**) but focused on the structure at and around M2225/M2241 (wildtype human and mouse channels overlaid). M2225R is human Piezo1 in which methionine (M) is replaced by arginine (R) at position 2225. M2241A is mouse Piezo1 in which methionine (M) is replaced by alanine (A) at position 2241. M2241R is mouse Piezo1 in which methionine (M) is replaced by arginine (R) at position 2241. Atoms from each residue indicated above in each Piezo1 subunit are shown as grey (carbon), blue (nitrogen) and yellow (sulphur) spheres.

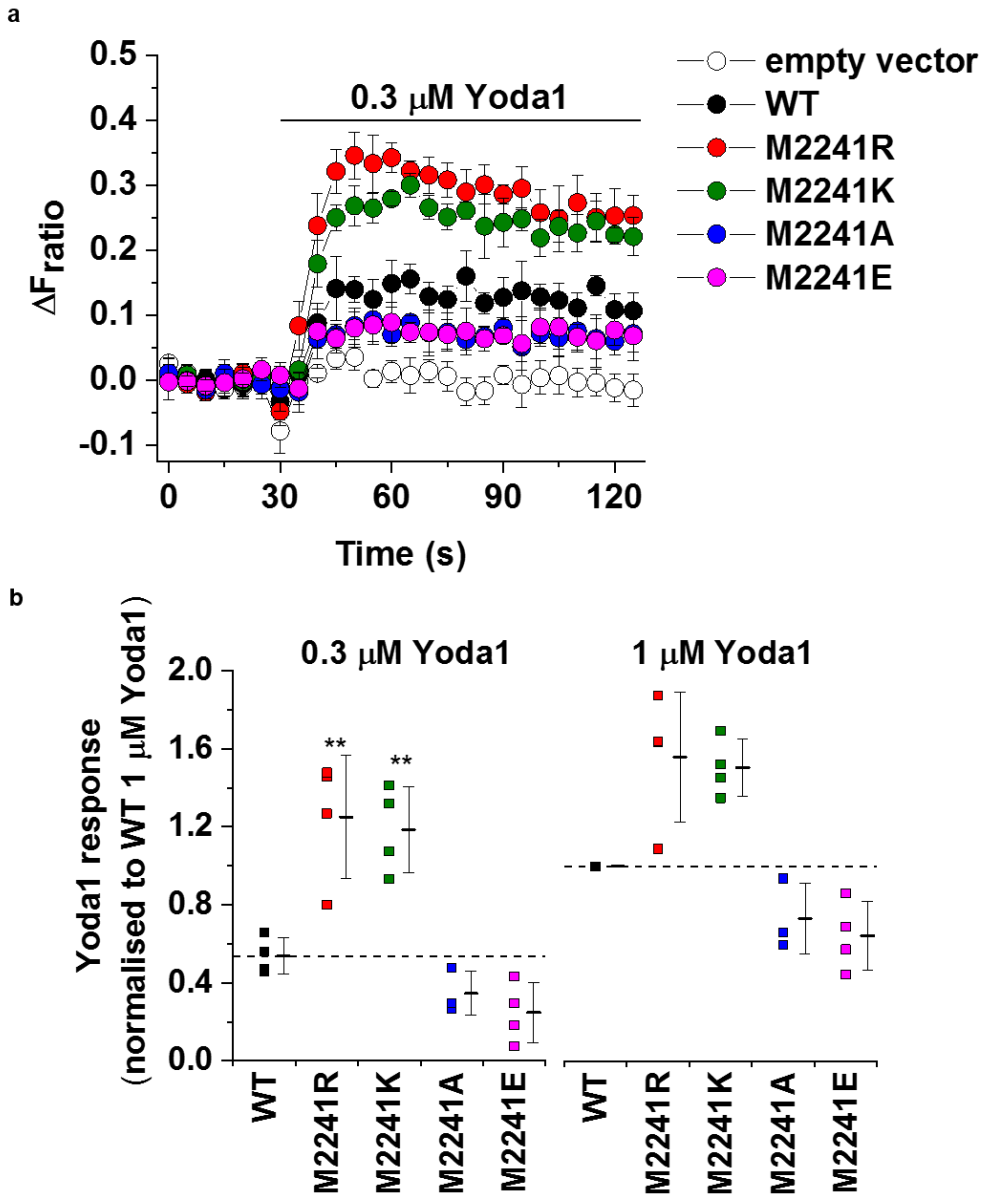

Figure S2. M2241R causes gain-of-function in mouse PIEZO1. (**a**) Exemplar intracellular Ca^{2+} measurement data for HEK 293 cells transiently transfected with wildtype (WT) murine PIEZO1 or PIEZO1 with the indicated mutations at position 2241. 30 s after the start of each recording, cells were exposed to 0.3 μM Yoda1. Ca^{2+} concentration is shown as increase above baseline (ΔCa^{2+}_i). Data are mean ± s.d (N=5 replicate wells were data point). (**b**) Summary analysis for experiments of the type shown in (**a**) in which responses to 0.3 μM Yoda1 or 1 μM Yoda1 were averaged over 30 s (30-60 s) after Yoda1 application. All individual data points are shown with mean ± s.d.: n = 4 (WT, M2241R, M2241K, M2241E) and n = 3 (M2241A). Statistical analysis was performed only on 0.3 μM Yoda1 data because all data were normalised to the WT 1 μM Yoda1 response. One-way ANOVA with post hoc Bonferroni test indicated significantly increased response to 0.3 μM Yoda1 in M2241R and M2241K (** $P < 0.01$).

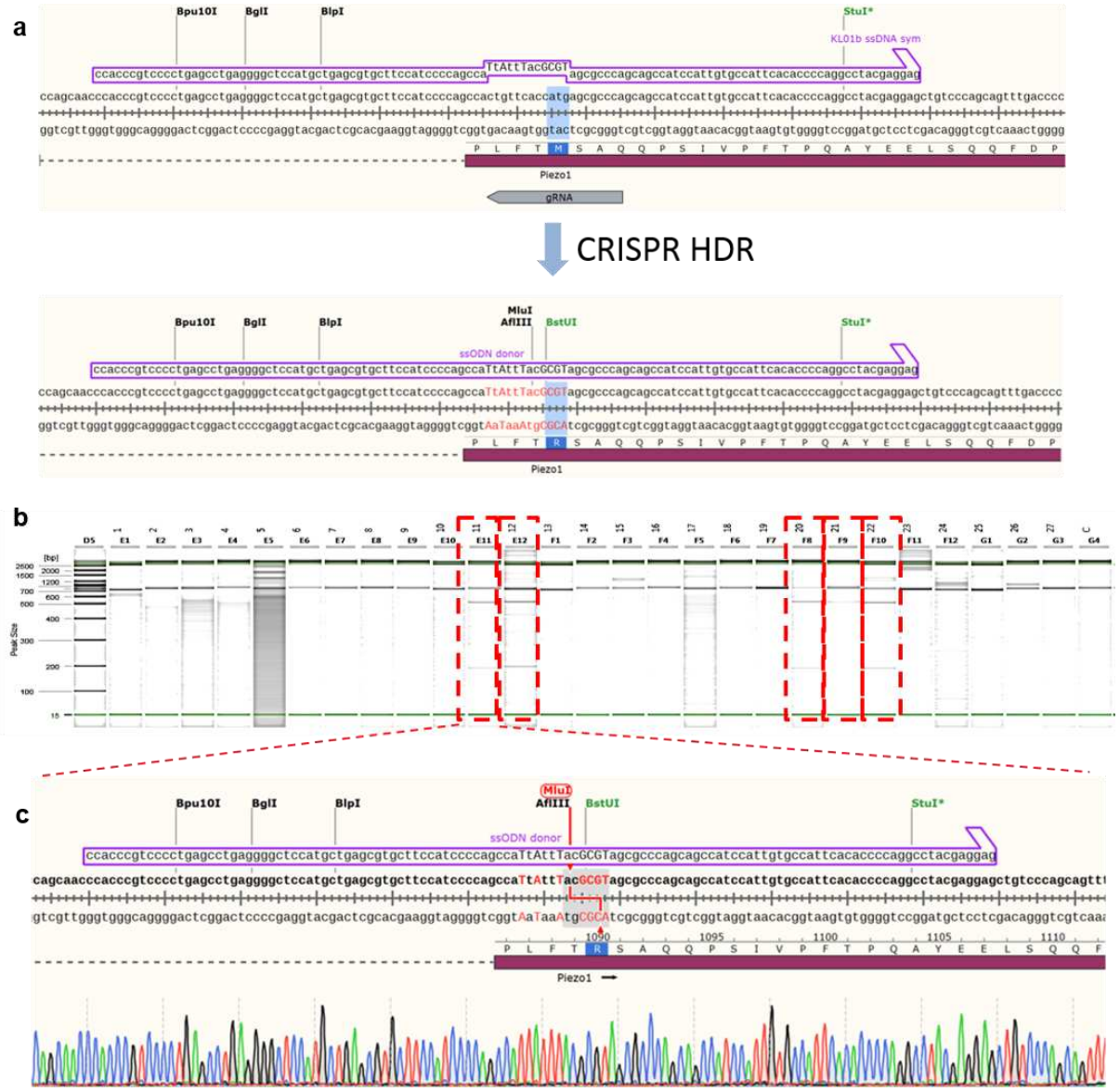

Figure S3. Generation of PIEZO1$^{M\text{-}R/M\text{-}R}$ mice. (**a**) CRISPR mutagenesis design, gRNA target sequence indicated by arrow below the highlighted M2241, and ssODN donor template indicated by purple arrow above the sequence (upper panel). Post CRISPR mediated HDR the red sequence is integrated, resulting in synonymous base changes and non-synonymous base changes resulting in M2241R. Also indicated is the creation of a MluI restriction site. (**b**) MluI digest of PCR amplified products from gDNA extracted from pups. Dashed red boxes indicated candidate pups likely harbouring the desired change. (**c**) Sanger sequencing of pup 11 as an example, showing perfect alignment with predicted post-HDR sequence.

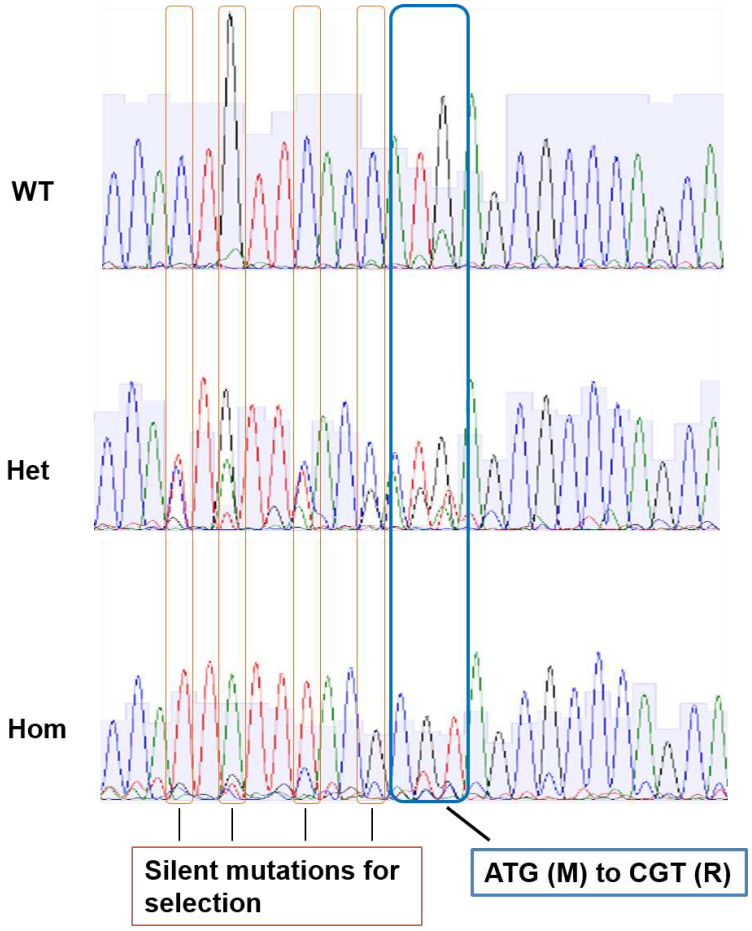

Figure S4. Sequence analysis of PIEZO1$^{M\text{-}R/M\text{-}R}$ mouse colony. Sanger sequencing of PCR amplicon indicating CRISPR-generated mutations by homology-directed repair. DNA sequence encoding methionine (ATG) to arginine (CGT) mutation are highlighted by the blue box. Silent mutations for MLU1 selection are highlighted by the orange boxes. In the sequencing trace, blue = cysteine, green = adenine, red = thymine, black = guanine.

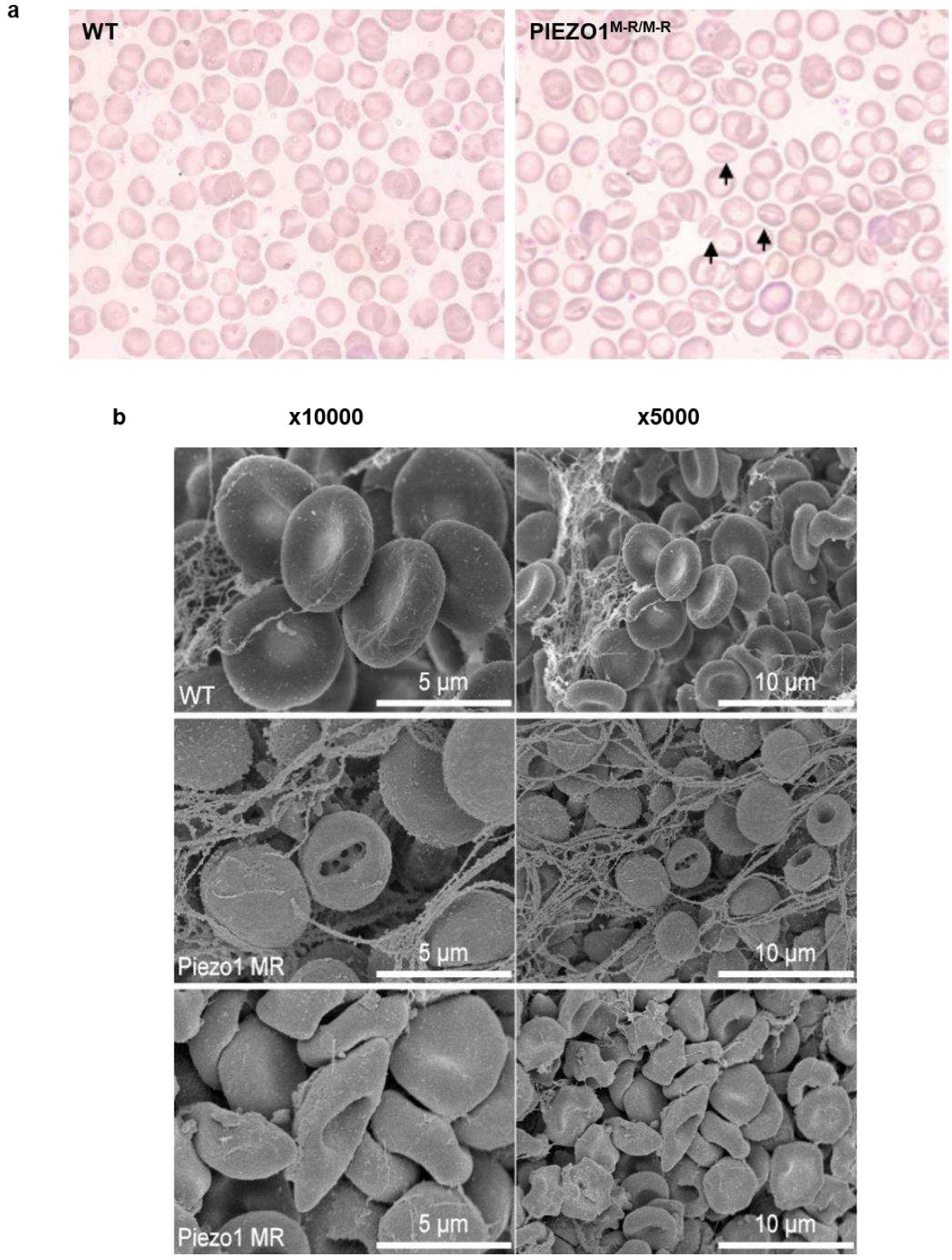

Figure S5. Stomatocytosis. (**a**) RBCs from wildtype mice (WT, left) and PIEZO1$^{M\text{-}R/M\text{-}R}$ mice (right) were investigated with May-Grunwald and Giesma stains. Magnification was 100 times. The presence of stomatocytes is indicated by the black arrows in the PIEZO1$^{M\text{-}R/M\text{-}R}$ image. (**b**) Scanning electron microscopy images of RBCs from WT (1 example at 2 magnifications) and PIEZO1$^{M\text{-}R/M\text{-}R}$ (2 examples at 2 magnifications: "Piezo1 MR") mice, showing presence of stomatocytes in PIEZO1$^{M\text{-}R/M\text{-}R}$ mice. Representative of 2 independent experiments.

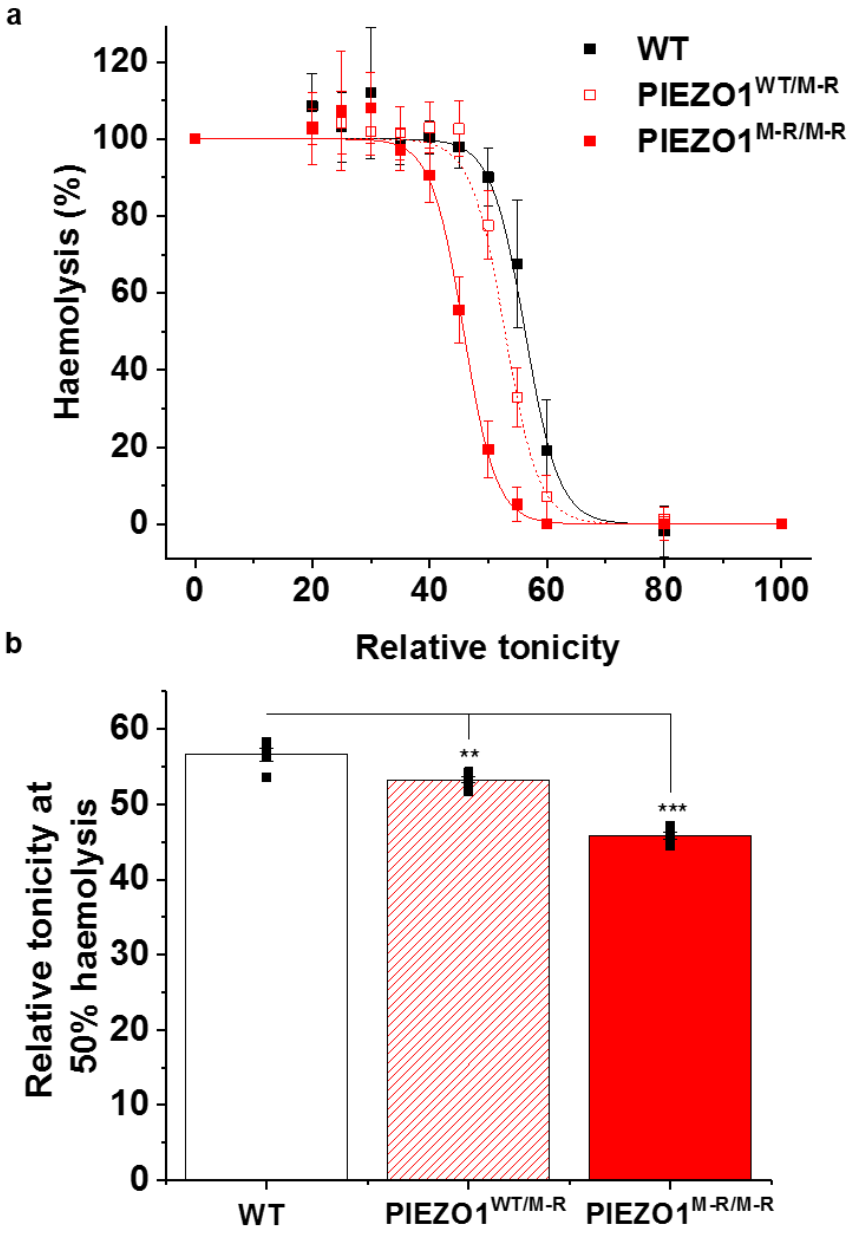

Figure S6. Reduced osmotic fragility. (**a**) Osmotic fragility test in RBCs from WT, PIEZO1$^{WT/M-R}$ and PIEZO1$^{M-R/M-R}$ mice. Data are shown as mean ± s.d (n = 5, 6 and 5 respectively). (**b**) Analysis for data of the type shown in (**a**) to indicate the tonicity at which 50 % of the RBCs were lysed, calculated from fitted curves to each individual data set, as exemplified in (**a**). Each data point represents a value from an independent experiment with mean values and error bars representing s.d.. Statistical analysis was by one-way ANOVA with post hoc Bonferroni test: ** $P < 0.01$ and *** $P < 0.001$.

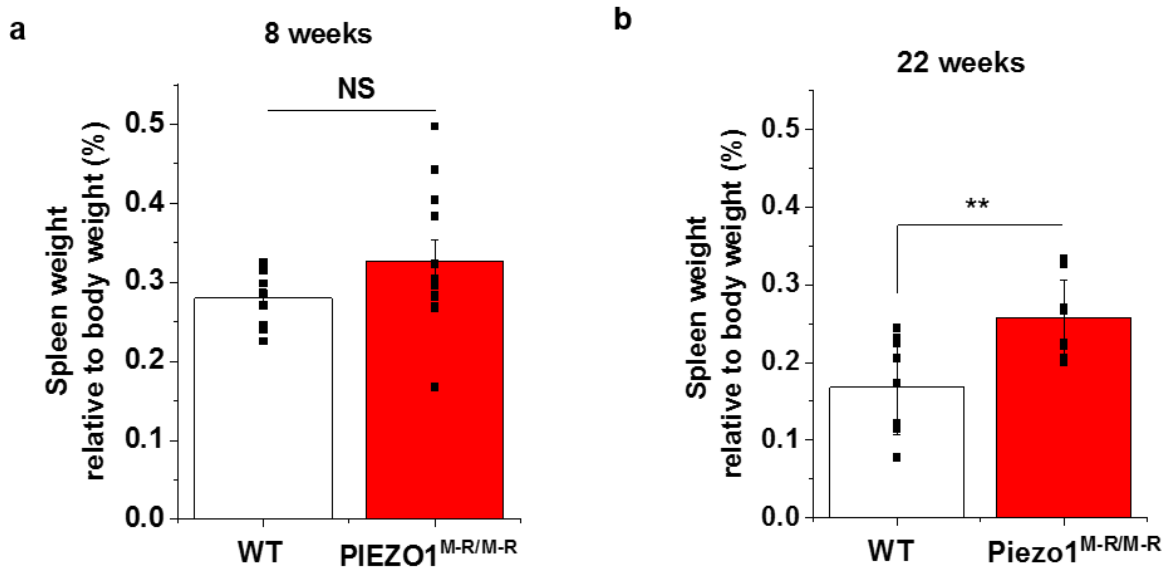

Figure S7. Increased spleen weight. (**a**) Mean ± s.d. weight of spleen as a percentage of total body weight in 8 week-old mice: n = 10 wildtype (WT) and n = 12 PIEZO1$^{M\text{-}R/M\text{-}R}$. NS: not significantly different. (**b**) Mean ± s.d. weight of spleen as a percentage of total body weight in 22 week-old mice (n = 9 for each genotype; ** $P < 0.01$).

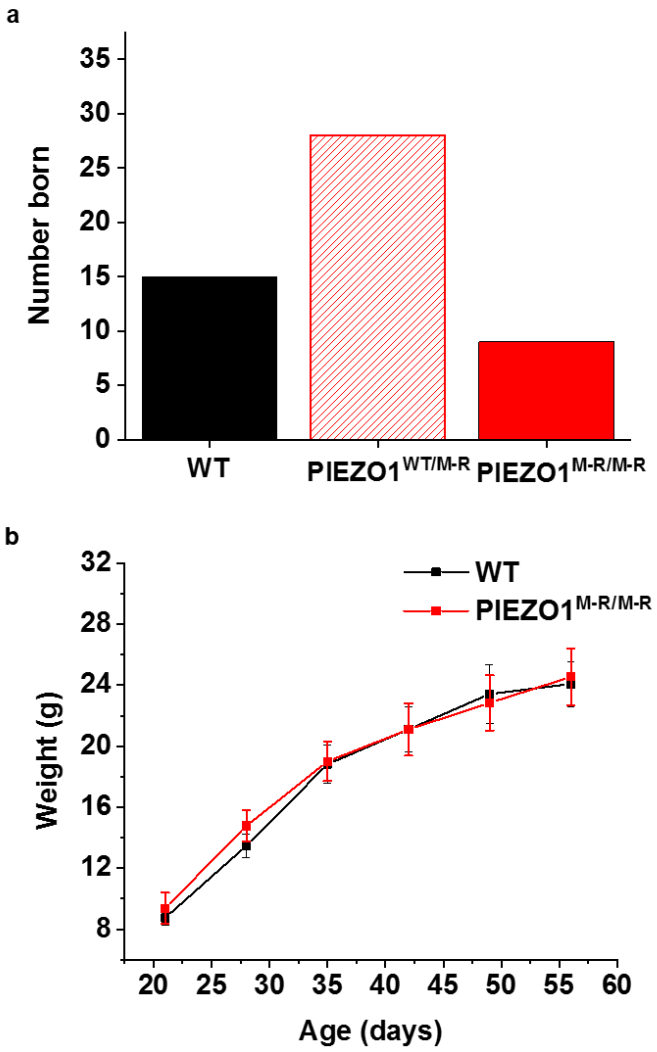

Figure S8. Birth numbers and weight gain in adults. (**a**) Numbers of mice born with the indicated genotypes after mating of PIEZO1$^{WT/M-R}$ mice. (**b**) Mean ± s.d. comparison of body weights of wildtype (WT) and PIEZO1$^{M-R/M-R}$ mice between 3-8 weeks of age (n = 5 WT, n = 7 PIEZO1$^{M-R/M-R}$).

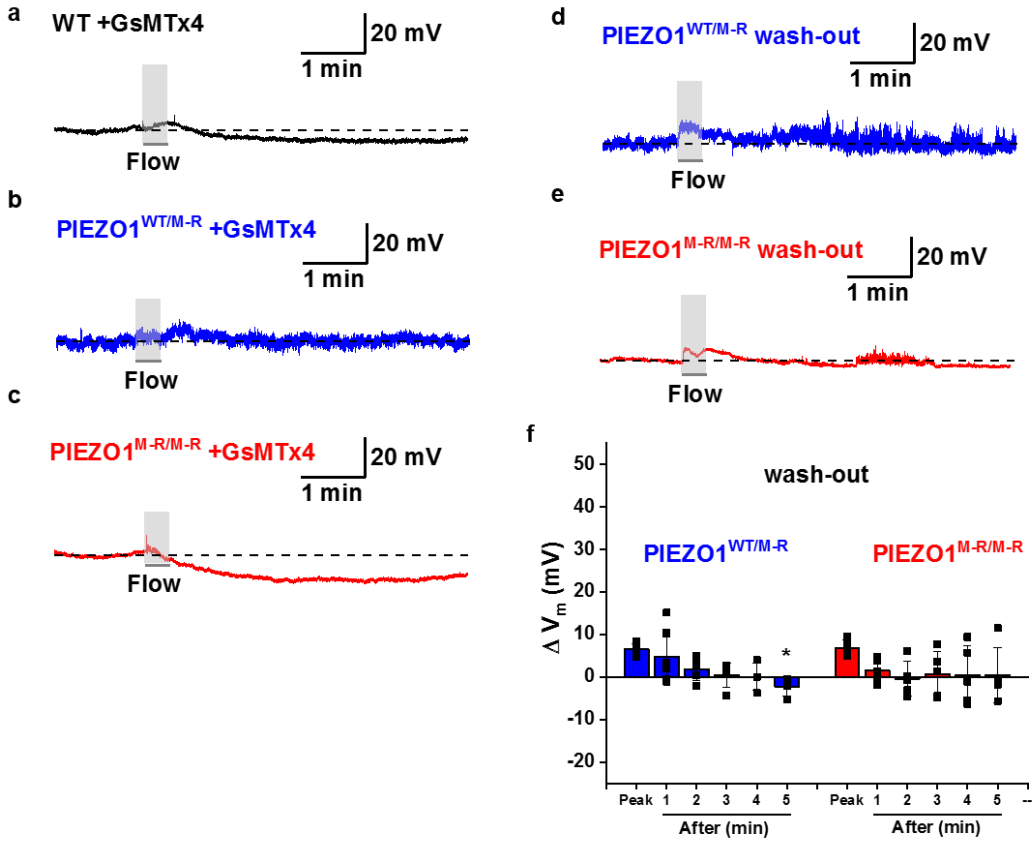

Figure S9. Effect of GsMTx4 on membrane potential responses. (**a-c**) Exemplar membrane potential (V_m) recordings obtained using perforated-patch whole-cell mode applied to freshly-isolated RBCs from wildtype (WT) (**a**), PIEZO1$^{WT/M-R}$ (**b**) or PIEZO1$^{M-R/M-R}$ mice (**c**) in the continuous presence of 2.5 μM GsMTx4. Mean data are shown in Figure 1e. (**d**, **e**) As for (**b**, **c**) but after at least 30 min wash-out of GsMTx4. (**f**) Mean ± s.d. data for experiments of the type shown in (**d**, **e**). All individual data points are superimposed. n = 6 (max, 1 min), 5 (2 and 3 min), 4 (4 and 5 min) for PIEZO1$^{WT/M-R}$ and n =5 for PIEZO1$^{M-R/M-R}$. Statistical analysis by one-way ANOVA with Bonferroni's post-hoc test indicated significant decay of the PIEZO1$^{WT/M-R}$ response at 5 min compared with Peak (P * <0.05).

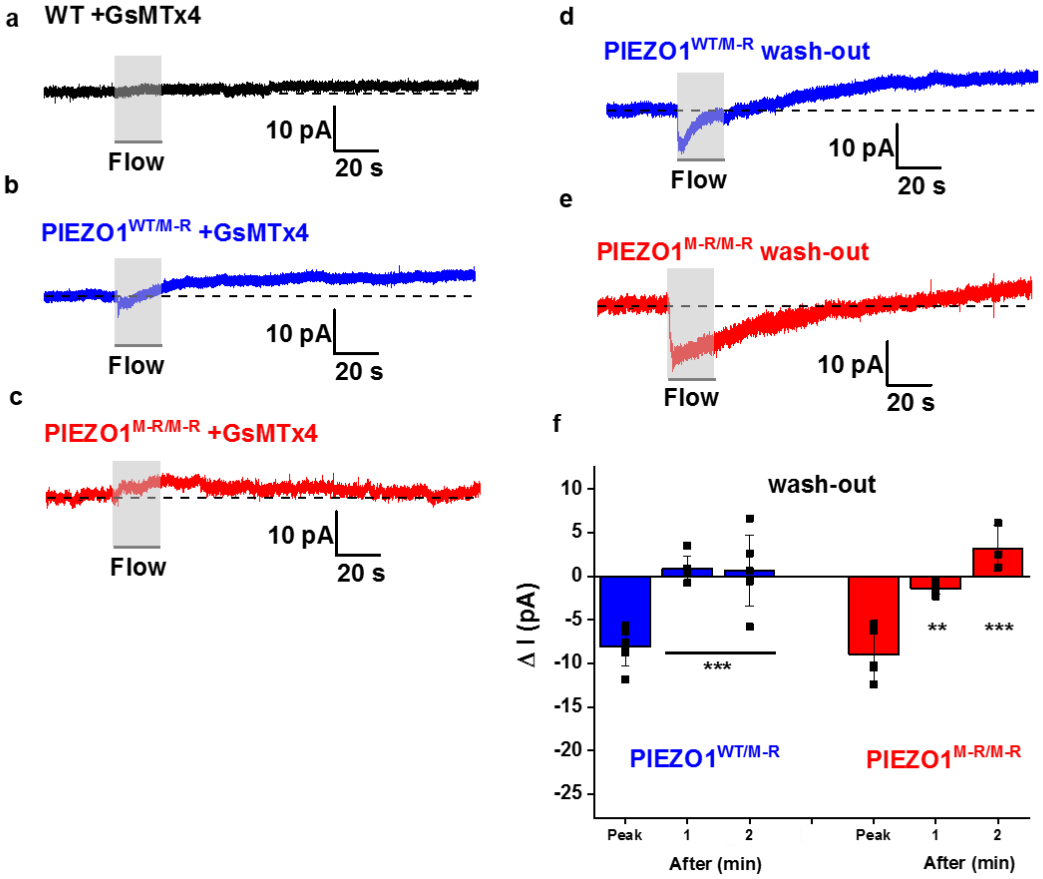

Figure S10. Effect of GsMTx4 on membrane current responses. (**a-c**) Exemplar ionic current recordings obtained using perforated-patch technique in whole-cell voltage-clamp mode applied to freshly-isolated RBCs from wildtype (WT) (**a**), PIEZO1$^{WT/M-R}$ (**b**) or PIEZO1$^{M-R/M-R}$ mice (**c**) in the continuous presence of 2.5 µM GsMTx4. Mean data are shown in Figure 1j. (**d**, **e**) As for (**b**, **c**) but after at least 30 min wash-out of GsMTx4. (**f**) Mean ± s.d. data for experiments of the type shown in (**d**, **e**). All individual data points are superimposed. n = 6 for PIEZO1$^{WT/M-R}$ and n = 5 (max, 1 min), 3 (2 min) for PIEZO1$^{M-R/M-R}$. Statistical analysis by one-way ANOVA with Bonferroni's post-hoc test indicated significant decay of the PIEZO1$^{WT/M-R}$ and PIEZO1$^{M-R/M-R}$ responses at 1 and 2 min compared with Peak (P ** <0.01 or *** P < 0.001).

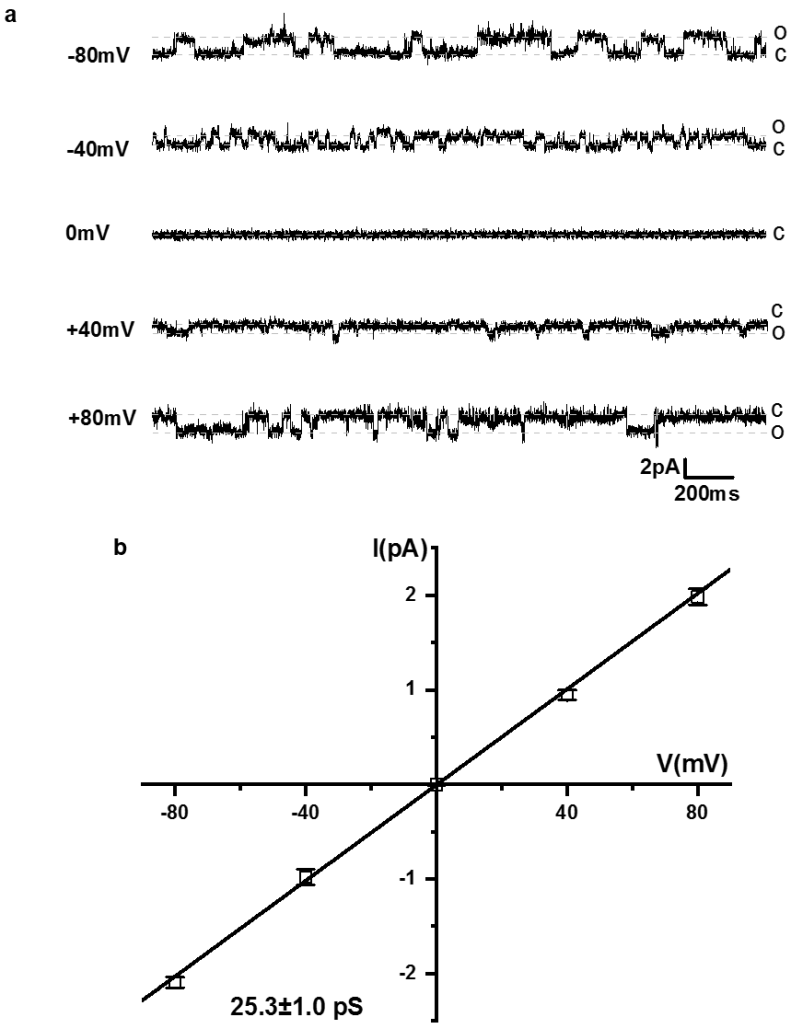

Figure S11. Unitary current-voltage (I-V) analysis. Single channel activity measured by cell-attached patch technique applied to freshly-isolated RBCs of PIEZO1$^{WT/M-R}$ mice. (**a**) Exemplar single channel activity at 5 voltages, as indicated to the left of each trace. Dotted horizontal lines indicate open (O) and closed (C) channel states. Activity was measured after a pressure pulse to -80 mmHg. (**b**) Mean ± s.d. unitary current amplitude plotted against voltage for 5 independent experiments. A straight line was fitted to each set of data points, indicating channel conductance of 25.3 ± 1.0 pS, which is the expected value for PIEZO1 channels.

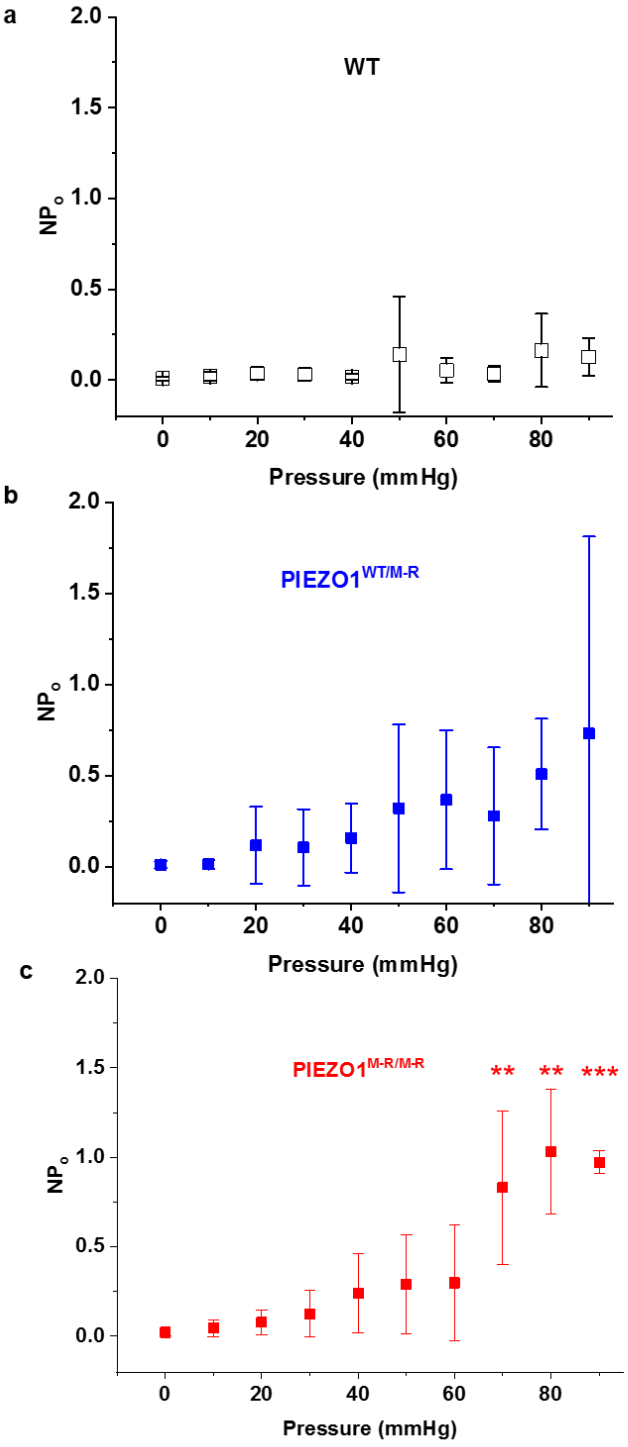

Figure S12. Single channel activity analysis. Single channel activity measured by cell-attached patch technique applied to freshly-isolated RBCs of wildtype (WT) (**a**), PIEZO1$^{WT/M-R}$ (**b**) or PIEZO1$^{M-R/M-R}$ mice (**c**, n=3) following pressure pulses to 0 - 90 mmHg for the full 12-s periods as exemplified in the traces of Figure 2a, c, e and g. Mean ± s.d. NP_o (channel number multiplied by open probability) is plotted against the amplitude of the pressure pulse applied before measuring the activity. Statistical analysis by one-way ANOVA with Bonferroni's post-hoc test indicated significant increase in NP_o of PIEZO1$^{M-R/M-R}$ but not WT or PIEZO1$^{WT/M-R}$ at 70, 80 and 90 mmHg compared with 0 mmHg (P ** <0.01 or *** P < 0.001).

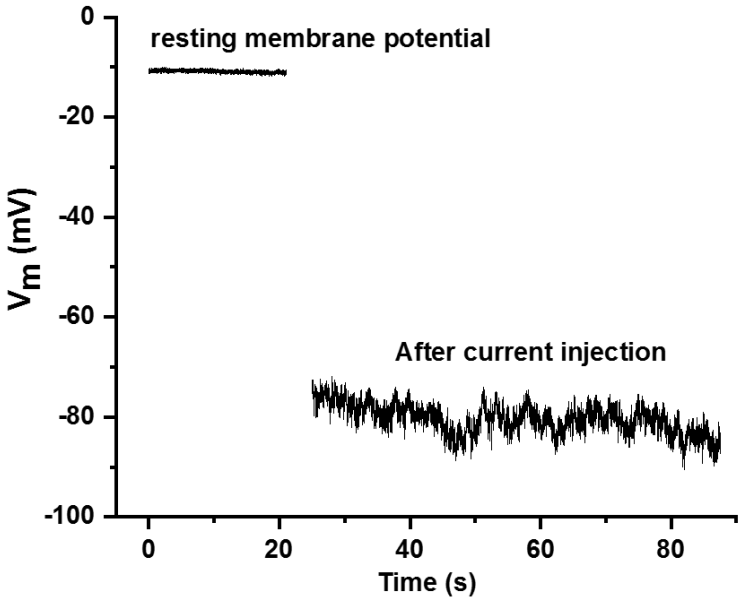

Figure S13. Membrane potential setting to -80 mV. Exemplar measurement to illustrate the technical approach for membrane potential recordings. Shown are blocks of trace for the RBC resting membrane potential prior to current injection and the new membrane potential set to approximately -80 mV by current injection from the patch pipette.

	WT **Mean ± SD**	**PIEZO1$^{M\text{-}R/M\text{-}R}$** **Mean ± SD (P value vs WT)**
HGB (g/L)	**129.60 ± 2.30**	**121.50 ± 2.65 (0.002**)**
WBC (10^9 cells/L)	**2.50 ± 0.61**	**2.945 ± 1.20 (0.50)**
WBCP (10^9 cells/L)	**2.39 ± 0.52**	**2.81 ± 1.24 (0.50)**
PLT (10^9 cells/L)	**861.20 ± 108.66**	**861.5 ± 106.83 (0.99)**
MCV (fL)	**50.64 ± 0.95**	**49.90 ± 1.08 (0.31)**
HCT (L/L)	**0.45 ± 0.01**	**0.41 ± 0.01 (0.003**)**
RBC (10^{12} cells/L)	**8.88 ± 0.14**	**8.32 ± 0.43 (0.03*)**
MCH (pg)	**14.60 ± 0.19**	**14.63 ± 0.74 (0.94)**
MCHC (g/L)	**288.24 ± 8.28**	**293.18 ± 10.51 (0.45)**
CHCM (g/L)	**282.40 ± 8.91**	**292.50 ± 9.15 (0.14)**
RDW (%)	**11.74 ± 0.27**	**14.18 ± 0.43 (0.00002***)**
HDW (g/L)	**16.56 ± 0.98**	**19.40 ± 1.31 (0.007**)**
%RETIC	**4.27 ± 0.79**	**7.33 ± 0.78 (0.002**)**

Table S1. Haematological parameters. Mean ± s.d. data and p-values for haematological parameters comparing WT (n = 4) and PIEZO1$^{M\text{-}R/M\text{-}R}$ (n = 5) mice: HGB, Haemoglobin; WBC, White blood cells; WBCP, White Blood Cell Count from the Peroxidase Method; PLT, Platelet Count; MCV, Mean Corpuscular Volume; HCT, Haematocrit; RBC, Red Blood Cells; MCH, Mean Corpuscular Haemoglobin; MCHC, Mean Corpuscular Haemoglobin Concentration; CHCM, Cellular Haemoglobin Concentration Mean; RDW, Red Blood Cell Distribution Width; HDW, Haemoglobin Concentration Distribution Width; %RETIC, percentage of reticulocytes. Statistically significant differences are indicated by *P < 0.05; **P < 0.01 and ***P < 0.001 (Student's t-tests).

	Mean ± SD		P value vs WT
	WT	PIEZO1$^{M\text{-}R/M\text{-}R}$	
ALBP (g/L)	**13.04 ± 1.65**	**13.22 ± 0.50**	**0.82**
ALP_2c (U/L)	**146.68 ± 22.23**	**127.36 ± 23.55**	**0.24**
ALT_c (U/L)	**33.84 ± 7.14**	**32.10 ± 8.27**	**0.73**
IRON_2 (mMol/L)	**18.98 ± 3.61**	**20.02 ± 3.96**	**0.68**
TIBC (mMol/L)	**21.72 ± 27.66**†	**38.46 ± 29.98**	**0.39**
Transferrin (mg/mL)	**2.22 ± 0.18**	**2.56 ± 0.27**	**0.0051***

Table S2. Liver function and iron tests. Liver function tests: ALBP, albumin; ALP-2c, alkaline phosphatase; ALT-c, alanine aminotransferase; TIBC, total iron binding capacity. Data are shown as mean ± s.d. (n = 5 mice in each group except for the transferrin data, which are for n = 8 WT mice and n = 12 PIEZO1$^{M\text{-}R/M\text{-}R}$ mice). †The analysis included 3 values that could only be determined as <8.4 μMol/L and the number 8.4 was used (see Source Data). Statistically significant differences are indicated by *P < 0.05 (Student's t-tests).

SUPPLEMENTAL REFERENCES

1. Guo YR, MacKinnon R. Structure-based membrane dome mechanism for Piezo mechanosensitivity. *eLife*. 2017;6:e33660.

2. Carella M, Stewart G, Ajetunmobi JF, et al. Genomewide Search for Dehydrated Hereditary Stomatocytosis (Hereditary Xerocytosis): Mapping of Locus to Chromosome 16 (16q23-qter). *The American Journal of Human Genetics*. 1998;63(3):810-816.

3. Zheng W, Gracheva EO, Bagriantsev SN. A hydrophobic gate in the inner pore helix is the major determinant of inactivation in mechanosensitive Piezo channels. *Elife*. 2019;8.

4. De Vecchis D, Beech DJ, Kalli AC. Molecular principles of Piezo1 activation by increased membrane tension. *bioRxiv*. 2019;823518(https://doi.org/10.1101/823518).

5. Bae C, Gnanasambandam R, Nicolai C, Sachs F, Gottlieb PA. Xerocytosis is caused by mutations that alter the kinetics of the mechanosensitive channel PIEZO1. *Proceedings of the National Academy of Sciences*. 2013;110(12):E1162-E1168.

6. Glogowska E, Schneider ER, Maksimova Y, et al. Novel mechanisms of PIEZO1 dysfunction in hereditary xerocytosis. *Blood*. 2017;130(16):1845.

7. Albuisson J, Murthy SE, Bandell M, et al. Dehydrated hereditary stomatocytosis linked to gain-of-function mutations in mechanically activated PIEZO1 ion channels. *Nat Commun*. 2013;4:1884.

8. Rode B, Shi J, Endesh N, et al. Piezo1 channels sense whole body physical activity to reset cardiovascular homeostasis and enhance performance. *Nature Communications*. 2017;8(1):350.

9. Li J, Hou B, Tumova S, et al. Piezo1 integration of vascular architecture with physiological force. *Nature*. 2014;515(7526):279-282.

10. Ranade SS, Qiu Z, Woo SH, et al. Piezo1, a mechanically activated ion channel, is required for vascular development in mice. *Proc Natl Acad Sci U S A*. 2014;111(28):10347-10352.

11. Maneshi MM, Ziegler L, Sachs F, Hua SZ, Gottlieb PA. Enantiomeric Abeta peptides inhibit the fluid shear stress response of PIEZO1. *Sci Rep*. 2018;8(1):14267.

12. Syeda R, Florendo MN, Cox CD, et al. Piezo1 Channels Are Inherently Mechanosensitive. *Cell Rep*. 2016;17(7):1739-1746.

13. Hyman AJ, Tumova S, Beech DJ. Piezo1 Channels in Vascular Development and the Sensing of Shear Stress. *Curr Top Membr*. 2017;79:37-57.

14. Murthy SE, Dubin AE, Patapoutian A. Piezos thrive under pressure: mechanically activated ion channels in health and disease. *Nat Rev Mol Cell Biol*. 2017;18(12):771-783.

15. Lewis AH, Grandl J. Mechanical sensitivity of Piezo1 ion channels can be tuned by cellular membrane tension. *Elife*. 2015;4.

16. Wu J, Lewis AH, Grandl J. Touch, Tension, and Transduction – The Function and Regulation of Piezo Ion Channels. *Trends in Biochemical Sciences*. 2017;42(1):57-71.

17. Martins JR, Penton D, Peyronnet R, et al. Piezo1-dependent regulation of urinary osmolarity. *Pflügers Archiv - European Journal of Physiology*. 2016;468(7):1197-1206.

18. Peyronnet R, Martins JR, Duprat F, et al. Piezo1-dependent stretch-activated channels are inhibited by Polycystin-2 in renal tubular epithelial cells. *EMBO reports*. 2013;14(12):1143-1148.

19. Del Marmol JI, Touhara KK, Croft G, MacKinnon R. Piezo1 forms a slowly-inactivating mechanosensory channel in mouse embryonic stem cells. *Elife*. 2018;7.

20. Retailleau K, Duprat F, Arhatte M, et al. Piezo1 in Smooth Muscle Cells Is Involved in Hypertension-Dependent Arterial Remodeling. *Cell Reports*. 2015;13(6):1161-1171.

21. Blythe NM, Muraki K, Ludlow MJ, et al. Mechanically activated Piezo1 channels of cardiac fibroblasts stimulate p38 mitogen-activated protein kinase activity and interleukin-6 secretion. *J Biol Chem*. 2019.

22. Beech DJ, Kalli AC. Force Sensing by Piezo Channels in Cardiovascular Health and Disease. *Arterioscler Thromb Vasc Biol*. 2019:ATVBAHA119313348.

23. Bae C, Sachs F, Gottlieb PA. The mechanosensitive ion channel Piezo1 is inhibited by the peptide GsMTx4. *Biochemistry*. 2011;50(29):6295-6300.

24. Dyrda A, Cytlak U, Ciuraszkiewicz A, et al. Local membrane deformations activate Ca^{2+}-dependent K+ and anionic currents in intact human red blood cells. *PLoS One*. 2010;5(2):e9447.

25. Johnson RM, Tang K. Induction of a Ca^{2+}-activated K^+ channel in human erythrocytes by mechanical stress. *Biochim Biophys Acta*. 1992;1107(2):314-318.

26. Picard V, Guitton C, Thuret I, et al. Clinical and biological features in PIEZO1-hereditary xerocytosis and Gardos channelopathy: a retrospective series of 126 patients. *Haematologica*. 2019;104(8):1554-1564.

27. Zarychanski R, Schulz VP, Houston BL, et al. Mutations in the mechanotransduction protein PIEZO1 are associated with hereditary xerocytosis. *Blood*. 2012;120(9):1908-1915.

28. Ma S, Cahalan S, LaMonte G, et al. Common PIEZO1 Allele in African Populations Causes RBC Dehydration and Attenuates Plasmodium Infection. *Cell*. 2018;173(2):443-455 e412.

29. Rooks H, Brewin J, Gardner K, et al. A gain of function variant in PIEZO1 (E756del) and sickle cell disease. *Haematologica*. 2019;104(3):e91-e93.

30. Rotordam MG, Fermo E, Becker N, et al. A novel gain-of-function mutation of Piezo1 is functionally affirmed in red blood cells by high-throughput patch clamp. *Haematologica*. 2019;104(5):e179-e183.

31. Cahalan SM, Lukacs V, Ranade SS, Chien S, Bandell M, Patapoutian A. Piezo1 links mechanical forces to red blood cell volume. *Elife*. 2015;4.

32. Fotiou E, Martin-Almedina S, Simpson MA, et al. Novel mutations in PIEZO1 cause an autosomal recessive generalized lymphatic dysplasia with non-immune hydrops fetalis. *Nat Commun*. 2015;6:8085.

33. Lukacs V, Mathur J, Mao R, et al. Impaired PIEZO1 function in patients with a novel autosomal recessive congenital lymphatic dysplasia. *Nat Commun*. 2015;6:8329.

34. Syeda R, Xu J, Dubin AE, et al. Chemical activation of the mechanotransduction channel Piezo1. *Elife*. 2015;4.

35. Evans EL, Cuthbertson K, Endesh N, et al. Yoda1 analogue (Dooku1) which antagonizes Yoda1-evoked activation of Piezo1 and aortic relaxation. *British journal of pharmacology*. 2018;175(10):1744-1759.

36. Sali A, Blundell TL. Comparative protein modelling by satisfaction of spatial restraints. *J Mol Biol*. 1993;234(3):779-815.

37. Fiser A, Do RK, Sali A. Modeling of loops in protein structures. *Protein Sci*. 2000;9(9):1753-1773.

38. Shen MY, Sali A. Statistical potential for assessment and prediction of protein structures. *Protein Sci*. 2006;15(11):2507-2524.

39. Abraham MJ. GROMACS: High performance molecular simulations through multi-level parallelism from laptops to supercomputers. *SoftwareX*;1-2:19-25.

40. Huang J, MacKerell AD, Jr. CHARMM36 all-atom additive protein force field: validation based on comparison to NMR data. *J Comput Chem*. 2013;34(25):2135-2145.

41. Boutet E, Lieberherr D, Tognolli M, et al. UniProtKB/Swiss-Prot, the Manually Annotated Section of the UniProt KnowledgeBase: How to Use the Entry View. *Methods Mol Biol*. 2016;1374:23-54.

42. Notredame C, Higgins DG, Heringa J. T-Coffee: A novel method for fast and accurate multiple sequence alignment. *J Mol Biol*. 2000;302(1):205-217.

43. Dunbrack RL, Jr. Rotamer libraries in the 21st century. *Curr Opin Struct Biol*. 2002;12(4):431-440.

44. Pettersen EF, Goddard TD, Huang CC, et al. UCSF Chimera--a visualization system for exploratory research and analysis. *J Comput Chem*. 2004;25(13):1605-1612.